

Automated Machine Learning Pipeline for Training and Analysis Using Large Language Models

Adam Lahouari¹, Jutta Rogal^{1,2}, and Mark E. Tuckerman^{1,3,4,5,6}

¹NYU, Department of Chemistry, New York, NY 10003, USA

²Initiative for Computational Catalysis, Flatiron Institute, NY 10010, USA

³NYU, Department of Physics, New York, NY 10003, USA

⁴Courant Institute of Mathematical Sciences, NYU, NY 10012, USA

⁵NYU-ECNU Center for Computational Chemistry, Shanghai 200062, China

⁶Simons Center for Computational Physical Chemistry, NYU, NY 10003, USA

*Correspondence: al9500@nyu.edu

September 29, 2025

Abstract

Machine learning interatomic potentials (MLIPs) have become powerful tools to extend molecular simulations beyond the limits of quantum methods, offering near-quantum accuracy at much lower computational cost. Yet, developing reliable MLIPs remains difficult because it requires generating high-quality datasets, preprocessing atomic structures, and carefully training and validating models.

In this work, we introduce an Automated Machine Learning Pipeline (AMLPL) that unifies the entire workflow from dataset creation to model validation. AMLPL employs large-language-model agents to assist with electronic-structure code selection, input preparation, and output conversion, while its analysis suite (AMLPL-Analysis) based on ASE supports a range of molecular simulations. The pipeline is built on the MACE architecture and validated on acridine polymorphs, where with a straightforward fine-tuning of a foundation model mean absolute errors of 1.7 meV/atom in energies and 7.0 meV/Å in forces are achieved. The fitted MLIP reproduces DFT geometries with sub-Å accuracy and demonstrates stability during molecular dynamics simulations in the microcanonical and canonical ensemble.

1 Introduction

Molecular dynamics (MD) simulations are primarily employed to investigate finite-temperature effects, dynamical properties, and time-correlation functions in materials.[1, 2] While classical force fields enable access to long time and length scales, their inherent approximations can limit the accuracy of these predictions.[3] These classical force fields are often parameterized or fitted to specific types of systems or interactions, leading to inadequacies when attempting to generalize their use to broader, more complex scenarios. Particularly problematic is their inability to reliably distinguish subtle energy differences between closely related polymorphs, which typically differ by only a few kJ/mol.[4, 5] Such precision is critical in determining material stability, phase transitions, and reactive pathways, highlighting the need for methods that can accurately describe these delicate energy landscapes.

Quantum mechanical (QM) methods, such as Density Functional Theory (DFT) and post-Hartree-Fock approaches, offer high accuracy in capturing electronic structure details. However, their computational expense rapidly escalates with system size, making them impractical for routine simulations of large-scale molecular systems simulations.[6] This computational constraint limits their applicability to small or medium-sized systems.

In response to these limitations, machine learning interatomic potentials (MLIPs) have emerged as a robust alternative, bridging the accuracy of quantum chemical methods and the computational efficiency of classical force field potentials.[7, 8] MLIPs learn from quantum chemical data, providing high-fidelity representations of atomic interactions while remaining computationally efficient enough to handle large systems and dynamical simulations over longer timescales. They offer substantial improvements in both predictive accuracy and scalability, facilitating precise simulations of complex systems under a wide variety of conditions. However, having these benefits depends on the quality and comprehensiveness of the training dataset.

The key factor in developing an accurate model capable of effectively predicting user requirements lies in constructing a precise dataset. Initially, careful consideration of the underlying chemistry of the system is essential, particularly identifying the dominant interactions influencing system stability, such as long-range interactions for example. Subsequently, selecting the appropriate QM method is crucial. For instance, employing a plane-wave basis set is preferable over Gaussian basis sets when investigating crystalline structures, due to its better suitability for periodic systems.

Furthermore, it is crucial to ensure that the dataset contains structural configurations extending beyond the equilibrium minima. Typically, this sampling procedure begins with geometry optimization (or cell optimization in the case of crystals systems), followed by ab

initio molecular dynamics (AIMD) simulations conducted at various temperatures. In principle, such a protocol enables the dataset to sample a broad region of the potential energy surface (PES), capturing not only near-equilibrium configurations but also thermally accessible distortions, anharmonic vibrations, and local structural rearrangements. In practice, however, the extent of PES coverage is constrained by the timescales and temperature ranges explored during AIMD. For example, simulations at moderate temperatures primarily sample configurations near the equilibrium minima, whereas high-temperature trajectories can probe a wider basin of the PES, although at the cost of introducing highly distorted structures that may not be representative of typical conditions. The inclusion of these diverse structural samples significantly enhances the MLIP’s ability to generalize and adapt effectively across different simulation regimes, especially in MD scenarios. Conversely, a limited or inadequately constructed dataset covers only a narrow region of the PES, which can lead the model to learn spurious correlations and produce unrealistic or unreliable predictions outside the training domain.

Once the dataset is sufficiently comprehensive to handle diverse conditions, attention can be turned to selecting appropriate parameters for the training procedure. Recent developments in machine learning potentials increasingly rely on Graph Neural Networks (GNNs), which provide a natural way to represent atomic environments and have shown clear improvements in accuracy compared to earlier approaches.[9] In particular, the use of equivariant architectures—ensuring predictions respect rotational and translational symmetries—has further enhanced the reliability of these models.[10] To systematically evaluate such methods, large-scale benchmarking initiatives have emerged. The Matbench test suite provided a standardized benchmarks for inorganic materials properties,[11] and more recently, bench Discovery introduced a framework to assess machine learning predictions of crystal stability across vast chemical and structural spaces.[12] Extensive research efforts have already been devoted to developing large-scale benchmarks for molecular crystals, exemplified by the OMC25 dataset and its associated models, which aim to reproduce molecular properties with high fidelity.[13]

Examples of GNN-based MLIPs, such as MACE, have gained considerable attention.[14] MACE distinguishes itself through detailed modeling of atomic environments and provides foundational models pretrained across a broad spectrum of chemical systems. This approach significantly enhances predictive accuracy and reduces computational resources required during fine-tuning to specific use cases.[14, 15]

As training a potential from scratch can be highly resource-intensive and time-consuming, foundational models have become increasingly prevalent. These models are pre-trained on extensive datasets derived from thousands of DFT calculations. By leveraging these pre-

trained checkpoints, users can efficiently fine-tune models to their own datasets, benefiting from improved accuracy due to the foundational model’s existing chemical insights. Additionally, fine-tuning typically achieves faster convergence with fewer training epochs, requires less training data, and ensures robust performance due to prior exposure to diverse chemical environments. Despite these substantial advancements, the training, validation, and deployment of MLIPs continue to pose significant technical and practical challenges. The process typically demands extensive effort, as each aspect—from dataset preparation to model training and validation—requires attention and specific data formats compatible with various software packages.

To address these challenges, we introduce a comprehensive pipeline called Automated Machine Learning Pipeline (AMLP). AMLP simplifies the creation of MLIPs from straightforward input files, such as Crystallographic Information Files (`.cif`) or Cartesian coordinate files (`.xyz`). The AMLP pipeline comprises five distinct steps, each designed to streamline the overall process. Moreover, AMLP leverages Large Language Models (LLMs) to assist users in identifying suitable QM methodologies for their systems. In practice, the user provides a concise prompt describing the target system, and the LLM queries its knowledge of the published literature to suggest methods, basis sets, or dispersion corrections that have been successfully applied to similar cases. This capability not only offers an informed starting point for parameter selection but also helps the user rapidly survey prior research, thereby reducing the need for extensive manual literature review and enabling faster setup of reliable QM calculations. Subsequently, AMLP facilitates the automated creation of input files necessary for geometry optimization and AIMD simulations compatible with popular computational software such as Gaussian [16], VASP [17–20], and CP2K.[21]

Following simulations, AMLP systematically processes outputs into structured `.json` files, enabling convenient data storage, retrieval, and visualization of pertinent structural information. Finally, AMLP converts these processed datasets into HDF5 format, thereby facilitating seamless integration with ML training frameworks like MACE, further streamlining and simplifying the entire model-building workflow.

Furthermore, the AMLP methodology is designed to be user-friendly and accessible, requiring minimal coding expertise. Users simply specify a numerical input corresponding to the desired stage of the workflow, ensuring a straightforward and intuitive experience. The resulting potentials can subsequently be utilized through an analysis module, AMLP-Analysis, integrated with the Python-based Atomic Simulation Environment (ASE), facilitating flexible evaluation and simulation tasks.[22]

2 Code architecture

2.1 General flow chart of the AMLP pipeline

The complete AMLP workflow integrates a multi-agent LLM system with automated computational processes to create a pipeline from structure input to machine learning potential deployment. Algorithm 1 presents the overall architecture, which consists of two main components: (A) an automated data preparation pipeline that uses the multi-agent LLM recommendations to generate training datasets, and (B) post-training simulation tools that enable immediate application of the trained models. The pipeline is designed to minimize manual intervention.

The data preparation pipeline (Part A) has six sequential steps: structure parsing, LLM-guided method selection, quantum mechanical calculation setup, batch processing of results, automated AIMD generation, and final dataset formatting for MACE training.

Algorithm 1 Automated Machine Learning Pipeline (AMLP)

Input: `structure_file` (.xyz/.cif), `user_description`, `target_software`

Output: `mace_dataset`, `trained_model_tools`

```
1: // PART A: DATA PREPARATION PIPELINE
2: function AMLP_DATA_PIPELINE
3:   // Step 0: Structure Processing
4:   structure ← PARSE_STRUCTURE_FILE(structure_file)
5:   // Step 1: Multi-Agent LLM Method Selection
6:   qm_params ← LLM_METHOD_RECOMMENDATION(
7:     user_description, structure)
8:   // Step 2: Generate Initial Calculations
9:   calc_inputs ← GENERATE_CALCULATIONS(structure, qm_params)
10:  ▷ create single-point, geometry relaxation, cell optimization
11:  // Step 3: Process QM Outputs (Batch)
12:  qm_results ← PROCESS_ALL_QM_OUTPUTS(calc_inputs)
13:  // Step 4: Auto-Generate AIMD Inputs
14:  aimd_inputs ← CREATE_AIMD_FROM_QM(qm_results, qm_params)
15:  // Step 5: Process AIMD & Convert to MACE Format
16:  aimd_outputs ← PROCESS_AIMD_OUTPUTS(aimd_inputs)
17:  mace_dataset ← CONVERT_TO_MACE_FORMAT(
18:    aimd_outputs, qm_results)
19:  return mace_dataset
20: end function
21: // PART B: POST-TRAINING SIMULATION TOOLS
22: function SIMULATION_TOOLS(trained_mace_model)
23:   return simulation toolkit for MD, properties, optimization
24: end function
```

These steps allow users to easily utilize individual tools without needing to repeat the entire procedure. The initial step involves generating detailed feedback reports through AI-driven agents using a single user prompt as depicted in Algorithm 2, providing guidance on suitable QM methods to use and on the parameter settings for the investigated system. Subsequently, the second step facilitates automated input file generation, supporting various computational software options (CP2K, VASP, or Gaussian) for geometry or cell optimization. The third step dynamically processes simulation outputs from the chosen software, systematically extracting energies, forces, and coordinates, and formatting these into structured `.json` files. These `.json` files are instrumental in identifying global minima configurations, which subsequently enable the automatic creation of input files for AIMD simulations—constituting another key step in the workflow. Finally, by reprocessing both geometry optimization and AIMD simulation outputs, the pipeline generates HDF5 datasets in the format required by the current version of MACE. These files contain the training and validation data in a structure directly readable by the MACE training routines, completing the dataset preparation step. The use of HDF5 allows hierarchical storage of atomic configurations, energies, and forces in a single portable file. This makes the datasets not only compatible with MACE but also adapted for use in other codes that accept HDF5 inputs.

A tutorial that guides users through the general workflow is available online.[23] Even non-expert users can follow the steps to process single `.cif` files and construct a machine learning potential within a single session.

2.1.1 AI-agent feedback

The training procedure begins with AI-driven agents designed to provide users with tailored insights into their chemical systems, in line with their specific research objectives. These agents also offer an initial suggestion regarding the appropriate DFT code and parameter settings that may be suitable for their study. While LLMs are already being explored in the field of chemistry to generate insights from user queries, this area is still rapidly evolving due to its precision and ease of integration in different codes and workflows.[24]

Numerous efforts are underway to integrate LLMs into domain-specific computational frameworks.[25, 26] In our approach, we follow a similar paradigm by using an LLM-based model to suggest initial DFT setups. Additionally, we introduce an application of general-purpose AI tools, where queries are progressively refined and delegated to specialized agents tailored.

To use the AMLP framework, an account with an API platform of one of the current LLM providers is needed. Details on the setup with the latest LLM models are regularly

maintained and updated in the AMLP repository. We recommend using a model that provides a favorable balance between performance and cost-efficiency. The model selection can then be configured by editing a simple `config.yaml` file. Furthermore, each agent described below can be fine-tuned independently by specifying a distinct model and custom keywords suited to its specific role within the multi-agent framework.

The multi-agent system operates through a structured workflow where specialized agents collaborate to provide comprehensive quantum mechanical method recommendations. Initially, the AI agents engage with users interactively to collect detailed information about their objectives and requirements. The system then has a five-stage process: (1) query refinement to optimize the research question, (2) parallel literature analysis by experimental and theoretical chemistry specialists, (3) scientific integration of findings, (4) consultation with DFT software experts, and (5) synthesis of final recommendations. Algorithm 2 details this multi-agent coordination process, showing how each specialized agent contributes to the overall method selection workflow.

The literature review is implemented through the *PublicationAPI* class, which retrieves and analyzes publications from multiple databases, including arXiv[27], Crossref[28], PubMed[29], and Semantic Scholar[30]. These sources can be modified in the same configuration file where the agents’ models are defined. Parameter extraction relies primarily on LLM-based methods, with a fallback to regular expressions (Regex) if LLM parsing fails. Regex provides pattern-matching tools that locate, extract, and validate text based on predefined syntax. In this context, Regex serves as a backup for extracting computational details—such as DFT parameters—from scientific literature when AI-based extraction is unsuccessful.

The framework defines specialized chemistry agents. Two specialized agents are defined. The *ExperimentalChemistAgent* emphasizes keywords related to laboratory practice (experiment, synthesis, characterization, measurement, spectroscopy, microscopy, analysis), while the *TheoreticalChemistAgent* focuses on computational approaches (theory, simulation, computation, calculation, DFT, quantum, molecular dynamics, ab initio, functional). Each agent focuses on its respective domain—computational or experimental chemistry—using a relevance-ranking system. Publications are scored based on keyword matches in titles and abstracts (with weighted scoring), adjusted by a recency bonus for recent works. Review articles are prioritized to ensure broad coverage of the field, and queries are tailored to system-specific contexts (e.g., crystals, metals, organics, polymers). Users may also customize the keyword lists to fine-tune the search criteria for each agent. Finally, each agent compiles its findings into a report tailored to the user’s needs.

Upon approval from the supervisory agent, these refined reports are dispatched to specialized expert agents proficient in the widely utilized computational chemistry codes: VASP,

Algorithm 2 Multi-Agent LLM System for QM Method Selection

Input: `user_prompt`, `atomic_structure`

Output: `final_recommendation`, `literature_references`

```
1: function LLM_METHOD_RECOMMENDATION(user_prompt, atomic_structure)
2:   system_desc  $\leftarrow$  ANALYZE_STRUCTURE(atomic_structure)  $\oplus$  user_prompt
3:   // Initialize Specialized LLM Agents
4:   agents  $\leftarrow$  {EXPCHEM, THEOCHEM, GAUSSIAN,
5:     VASP, CP2K}
6:   supervisors  $\leftarrow$  {INTEGRATION, DFT_REC}
7:   // Step 1: Query Refinement Chain
8:   refined_query  $\leftarrow$  REFINE_QUERY(user_prompt, system_desc)
9:   // Step 2: Multi-Agent Literature Analysis
10:  exp_analysis  $\leftarrow$  agents.EXPCHEM.SUMMARIZE_REFS(refined_query)
11:  theo_analysis  $\leftarrow$  agents.THEOCHEM.SUMMARIZE_REFS(refined_query)
12:  // Step 3: Scientific Integration
13:  integrated_report  $\leftarrow$  supervisors.INTEGRATION.INTEGRATE(
14:    exp_analysis, theo_analysis)
15:  // Step 4: DFT Software Expert Consultation
16:  for expert  $\in$  {GAUSSIAN, VASP, CP2K} do
17:    expert_analysis[expert]  $\leftarrow$  agents.expert.ANALYZE_REFS(refined_query)
18:  end for
19:  // Step 5: Final Synthesis
20:  dft_content  $\leftarrow$  CONCATENATE(expert_analysis.values())
21:  final_rec  $\leftarrow$  supervisors.DFT_REC.INTEGRATE(dft_content)
22:  all_refs  $\leftarrow$  COMBINE_REFS(all_agent_outputs)
23:  return final_rec, all_refs
24: end function
```

Gaussian, and CP2K. Each of these expert agents provides detailed feedback and recommendations on the applicability and suitability of their respective codes for the user’s specific research needs.

Users first choose their preferred computational code based on expert feedback and receive guidance on appropriate parameter settings thanks to the reports. However, because LLM-based agents may fabricate data when source information is unavailable, a single incorrect output can propagate through the pipeline—creating chained dependencies in which one agent’s error misguides all subsequent agents. To guard against this cascading failure, we have strengthened each individual agent and our supervisory layer by implementing validation checkpoints and refining their prompts, thereby minimizing the risk of generating false information.

2.1.2 Input Generation

Based on the AI recommendations and user-defined parameters, input files are generated from `.cif` or `.xyz` formats. Two options are available:

1. **Batch-mode:** Automatically generates inputs for all structures using default templates.
2. **Guided-mode:** Allows users to specify DFT parameters interactively.

For example, in the VASP workflow, AMLP identifies all input structures (e.g. `.cif` or `xyz`) and prompts the user to define simulation cell size, functionals, cutoff energy, and other DFT parameters for all of them. The INCAR and KPOINTS files are automatically generated. It allows a step-by-step generation of the inputs for different structures at one time. Though template-driven, users are encouraged to verify all generated parameters. Minor discrepancies may exist depending on software versions, and basic familiarity with each package is recommended.

2.1.3 Output processing

Upon obtaining optimized molecular structures, users may proceed with the provided post-processing script, which is designed to extract recursively and organize essential computational outputs into a structured `.json` format. This includes atomic coordinates, total energies, atomic forces, elements, and simulation cell parameters (including cell lengths, angles, and volumes). Furthermore, the resulting `.json` file enables users to validate easily whether the optimization has properly converged and to identify any anomalies or errors that may have occurred during the simulation.

2.1.4 AIMD processing

The AIMD setup module begins by preprocessing the simulation output files. It systematically analyzes all `.json` files within a specified directory, detecting the atomic species in each file individually. For every system, it extracts the final geometry from the previous calculation and generates corresponding VASP or CP2K input files, incorporating user-defined parameters.

As in previous steps, AIMD simulation inputs are tailored to user specifications. A structured questionnaire interface allows users to explicitly define essential simulation parameters such as the target temperatures, integration timestep, and other relevant computational settings. For users less familiar with AIMD setups, the interface offers guidance to ensure

that simulation parameters—such as those approaching melting temperatures—are selected appropriately for the chemical system under study.

Although AIMD simulations are powerful tools for sampling diverse molecular configurations, it is strongly recommended to perform a post-simulation validation of selected structures using quantum chemical methods (e.g., Gaussian or VASP single-point calculations). This step ensures that the energies and geometries obtained from the AIMD trajectory are physically meaningful and suitable for further analysis or training purposes.

Upon completion of the AIMD simulations and subsequent evaluation of energies and forces, the output can be processed as with the last step, to produce temperature-specific `.json` datasets. These files serve as structured inputs for MLIP training or further electronic structure investigations.

2.1.5 ML potential dataset creation

The dataset containing all relevant information in a single `.json` file can be automatically converted into an HDF5 format, which is then partitioned into training and validation subsets—by default using an 85% to 15% split, although this ratio can be adjusted by the user. During this process, users are also prompted to define the batch size and specify a maximum threshold for atomic forces, which helps tailor the dataset to the intended training conditions. Any configurations exceeding this force threshold are automatically identified and excluded as outliers, thereby improving the robustness and physical relevance of the final dataset. Once the dataset is prepared, users can directly launch the training of a MLIP using the MACE architecture. A sample `config.yaml` file—containing all necessary parameters for training—is available in the project’s GitHub repository and can be adapted by users to suit their specific needs.[31] This ensures a straightforward transition from dataset generation to model training while preserving flexibility for methodological adjustments. Upon successful training, users obtain a customized MLIP, which can subsequently be directly loaded and utilized with the next module.

2.1.6 AMLP-A - Validation and Testing

This subsection enables users to load and apply their MLIP for a variety of computational analyses. The process is streamlined through a straightforward `config.yaml` configuration file, allowing users to conveniently execute multiple computational tasks simultaneously. This validation module uses ASE, a widely-used Python-based toolkit known for its simplicity, flexibility, and extensive range of features suitable for atomic-scale simulations.[22]

Users have several options for simulation types, including single-point energy calculations,

geometry optimizations and cell optimizations. Geometry optimization can be activated by setting the corresponding flag to in the `config.yaml` file. A variety of optimization algorithms provided by ASE, such as BFGS[32–35], LBFGS[36], and FIRE[37], are available for selection based on user preferences and requirements. Detailed information about these optimizers can be readily accessed through the ASE documentation.[38] Users must define an appropriate convergence criterion (f_{max}) to guide the optimization process. Upon successful completion of geometry optimization, the resulting data—including lattice parameters, total energy, simulation cell dimensions and angles, stress tensors, atomic coordinates, and individual atomic forces—are comprehensively reported and systematically saved into an `.xyz` file for further computational tasks.

Subsequent MD simulations can be performed. For simulations in the canonical (NVT) ensemble, users may employ either a Langevin[39] or a Nosé-Hoover thermostat[40, 41]. The Langevin integrator is particularly robust in dissipating excess energy and equilibrating systems with rugged potential energy surfaces, while the Nosé-Hoover chain integrator provides smoother canonical sampling without stochastic noise.

Alternatively, simulations may be conducted in the microcanonical (NVE) ensemble, in which the total energy is conserved. Here, the velocity-Verlet integrator is used to propagate the dynamics. Users can therefore choose between deterministic (Nosé-Hoover, velocity-Verlet) and stochastic (Langevin) schemes depending on the desired ensemble and level of control over thermal fluctuations. Energy conservation metrics are computed automatically for NVE runs to verify the stability of the integration. The energy conservation measure is calculated via

$$\Delta E = \frac{1}{N_{step}} \sum_{k=1}^{N_{step}} \frac{|E_k - E(0)|}{|E(0)|} \quad (1)$$

where $E(0)$ is the reference energy at the beginning of the analysis period (after equilibration), E_k is the total energy at step k , and N_{step} is the number of simulation steps up to the current point. This formulation provides a cumulative measure of energy conservation quality that accounts for all deviations from the initial energy, normalized by the reference energy.[42] Additionally, users can replicate the computational cell in multiple spatial dimensions to model larger systems and achieve more comprehensive statistical sampling.

From the final MD trajectories, the radial distribution function (RDF) $g(r)$ is computed using the `mdtraj` library.[43] The RDF is defined as

$$g(r) = \frac{1}{4\pi r^2 \rho N} \left\langle \sum_{i=1}^N \sum_{j \neq i}^N \delta(r - |\mathbf{r}_i - \mathbf{r}_j|) \right\rangle, \quad (2)$$

where ρ is the average number density, N is the number of atoms, and $\langle \cdot \rangle$ denotes an ensemble average. Users can specify whether the RDF is calculated globally or selectively for particular atomic pairs, such as nitrogen–nitrogen pairs, and RDFs calculated at different temperatures are collectively presented on a single plot to facilitate direct comparisons against the initial configuration.

This comprehensive computational framework gives users with the tools necessary to develop, rigorously validate, and utilize their MLIP effectively, as summarized in Figure 1. In the next section, we propose a case study where we exemplify the use of AMLP in order to create an MLIP for a specific crystal structure.

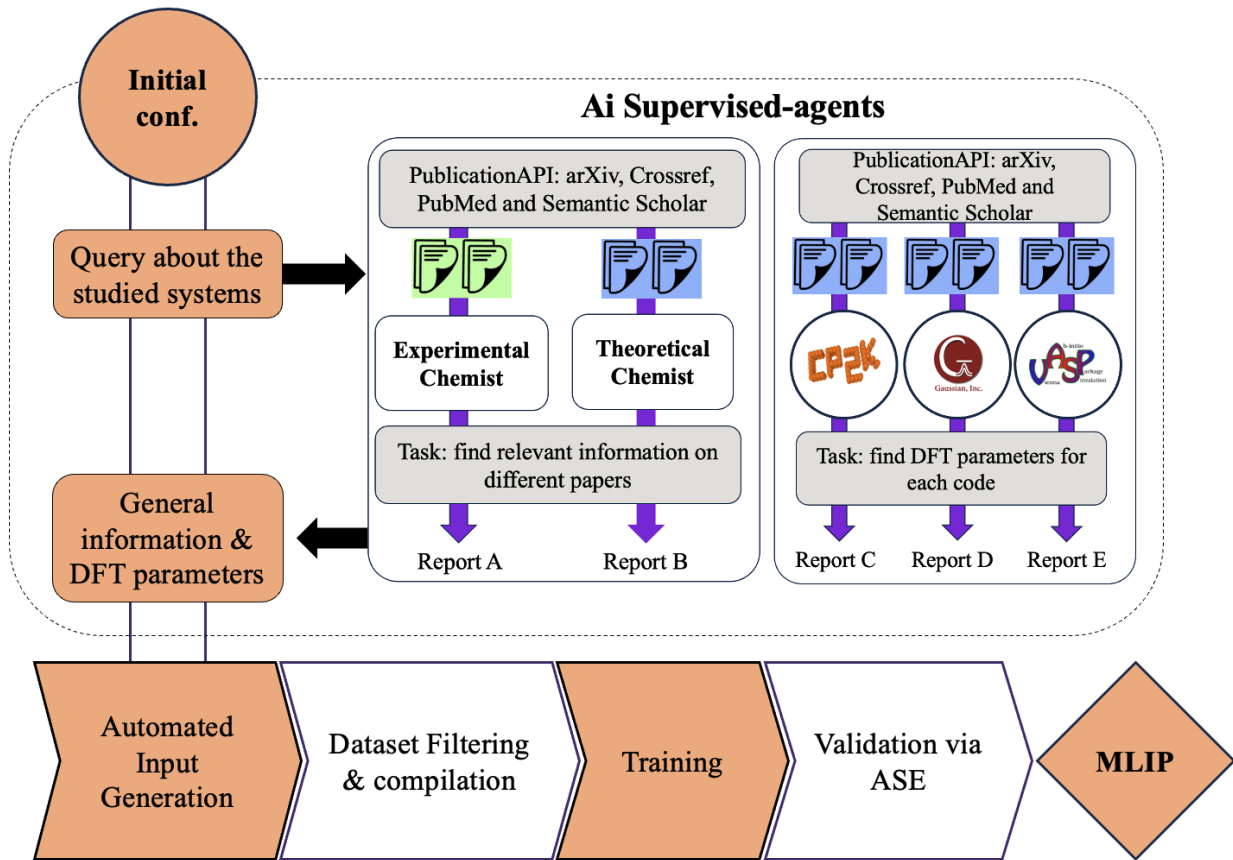


Figure 1: Roadmap of the Automated Machine Learning Potential (AMLP) framework. The workflow begins with structural inputs (`.xyz`, `.cif`), which are processed by AI supervised agents to extract relevant literature data and recommend DFT parameters for different codes (e.g., CP2K, Gaussian, VASP). Automated input generation produces ready-to-use files for geometry optimization, cell optimization, single point calculation and AIMD. Simulation outputs are curated into `.json` datasets containing energies, forces, and structural information, which are then used to train MLIPs. Validation via ASE includes geometry and cell optimization, MD simulations, RDF calculations. This roadmap illustrates the fully automated pipeline from raw input structures to validated MLIPs.

3 Case study

3.1 MLIPs for Acridine

We apply the new AMLP pipeline to acridine, a molecular crystal known to exhibit nine distinct crystal structures: eight polymorphs and one hydrate.[44] The primary challenge arises from their small lattice energy differences, typically within just a few kJ/mol.[45] Consequently, we seek to develop an MLIP capable of accurately distinguishing among the subtle structural variations of acridine polymorphs, thereby significantly improving predictive reliability compared to empirical force fields. All pure acridine polymorphs possess monoclinic symmetry, with experimental structures available from the Cambridge Structural Database (CSD) measured at room temperature. Due to variations in polymorph notation across different studies, we consistently adopt the naming convention provided by the CSD, as summarized in Table 1.

Table 1: Crystallographic data for acridine polymorphs

Polymorph	Space group	a (Å)	b (Å)	c (Å)	β (°)	V (Å ³)
ACRDIN04	P2 ₁ /n	11.25(1)	5.95(1)	13.60(1)	99.5(1)	898
ACRDIN05	Cc	6.17(2)	23.50(8)	12.87(4)	96.5(1)	1855
ACRDIN06	P2 ₁ /n	6.06(1)	22.81(4)	13.20(2)	95.9(1)	1815
ACRDIN09	P2 ₁ /c	6.05(7)	18.80(2)	16.20(2)	95.2(1)	1834
ACRDIN10	P2 ₁ /c	6.03(7)	18.76(2)	16.17(2)	95.2(1)	1821
ACRDIN11	P2 ₁ /n	11.18(5)	5.93(1)	13.59(4)	99.8(4)	889
ACRDIN12	P2 ₁ /n	11.28(1)	12.38(1)	6.68(1)	92.1(1)	933

Numerous theoretical studies have sought to determine the relative stability of acridine polymorphs.[44] However, classical force fields lack the flexibility required to accurately capture both the kinetic stability and the transitions between polymorphic forms.[46] Density Functional Theory (DFT) methods, while more accurate, still exhibit lattice-energy errors ranging from approximately 4.18 to 20 kJ/mol depending on the functional employed, whereas experimental energy differences between polymorphs rarely exceed 10 kJ/mol.[45] The MLIP developed here is trained on DFT data to reproduce the PES, thereby enabling simulations at larger system sizes and finite temperatures to explore polymorphic stability.

3.1.1 Dataset generation with LLMs

By launching the first option of the AMLP codes by the following single prompt, "I am developing a machine-learning interatomic potential for acridine polymorphs to predict energies,

forces, and thermodynamic properties across different conditions." We were able to obtain four different reports that are in the SI. These reports allowed us to garner insight into what has been done experimentally and theoretically on this kind of crystal structure. It gives information on what functionals and basis sets could be used to study crystalline forms for this system. Information regarding the importance of dispersion interactions is also noted.

Based on these considerations, we performed DFT calculations using the Perdew-Burke-Ernzerhof (PBE) functional[47] and a plane-wave basis set, as implemented in VASP, both of which were recommended by AMLP. The agents also suggested an electronic convergence threshold of 10^{-6} eV, which we adopted. For the plane-wave cutoff, AMLP proposed 500 eV; here, we employed a more tighter value of 850 eV to ensure accurate total-energy evaluations. With respect to Brillouin-zone sampling, no explicit recommendation was provided by the agents, and we therefore selected a Γ -centered $7 \times 7 \times 7$ Monkhorst-Pack mesh.[48] For the treatment of long-range dispersion interactions, AMLP advised at least the use of D3(BJ) corrections[49]; however, we opted for Grimme's D4 scheme,[50] which achieves accuracy comparable to the Many-Body Dispersion (MBD) method[51–53] while being substantially more efficient. The D4 correction ensures a reliable description of van der Waals interactions, which are essential for capturing the intermolecular forces governing crystal stability. All computational parameters are detailed in the SI. The crystal structures used in this study are presented in Table 1.

The DFT calculations of the eight polymorphs were subsequently processed using the AMLP code. The framework not only stores all relevant information in a structured `.json` format, as described in Section 2.1.3.

The reliability of the DFT calculations is evaluated by comparing the optimized unit-cell parameters and lattice energies against the corresponding experimental data from the CSD. The use of `.json` files further facilitates this process: by organizing data through easily readable keys, AMLP allows straightforward extraction and direct comparison of computed and experimental values. The DFT optimizations, performed at $T = 0$ K, result in a contraction of the unit cell volume by approximately 3% relative to the experimental structures determined near room temperature, which is expected due to the absence of thermal expansion. The DFT optimized and experimental volumes as well as relative difference

$$\Delta V = \frac{V_{\text{exp}} - V_{\text{theo}}}{V_{\text{exp}}}. \quad (3)$$

is shown together with the lattice energies

$$E_{\text{lattice}} = \frac{E_{\text{crystal}}}{Z} - E_{\text{gas}}, \quad (4)$$

in Figure 2.

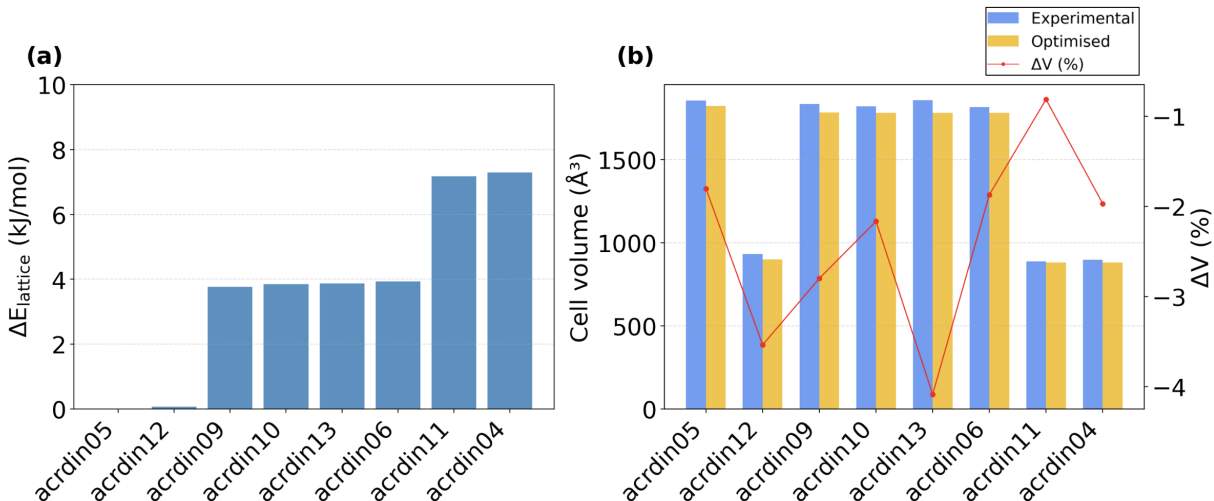


Figure 2: (a) ΔE denotes the difference in lattice energy between each polymorph and the most stable one (ACRDIN05). (b) Comparison between experimental (blue) and DFT optimized (yellow) unit-cell volumes of various acridine polymorphs. The red line corresponds to ΔV .

By examining the lattice-energy differences relative to the most stable polymorph (ACRDIN05), we find that the overall range is approximately 7.3 kJ/mol. As noted previously, even though ACRDIN05 appears as the lowest-energy form in our DFT calculations, this does not conclusively indicate that it is more stable than the others, since this range of lattice energies falls within the intrinsic error of DFT methods. Notably, the energy difference between ACRDIN05 and ACRDIN12 is only ~ 0.1 kJ/mol. A second group of four polymorphs (ACRDIN09, ACRDIN10, ACRDIN13, and ACRDIN06) has lattice energies higher by approximately 3.5 kJ/mol, only separated by 0.1 kJ/mol from one another. The lattice energies of the last two polymorphs, ACRDIN11 and ACRDIN04 are even higher by another 3 kJ/mol and again differ by only 0.1 kJ/mol. These results, together with the observed 3% cell contraction, support the accuracy of our optimized structures and their ability to reproduce experimentally relevant stability trends.

Following the cell optimizations, we carried out AIMD simulations with VASP across a temperature range of 300–800 K. This temperature range was specified interactively by using AMLP, to capture both room-temperature and high-temperature dynamical behavior, thereby ensuring that the potential remains transferable even under conditions approaching or exceeding the melting temperature. framework. Specifically, the code identifies the relevant `.json` file from the preceding cell-optimization step, extracts the most stable geometry, and prepares the corresponding AIMD setup. Users can specify the temperature range and

additional simulation parameters (e.g., timestep, ensemble), upon which AMLP automatically generates the corresponding input files. The analysis modules also provide default settings, ensuring that meaningful simulations can be carried out even without extensive user intervention.

For the present work, we employed the canonical (NVT) ensemble with a timestep of 1.0 fs over 10,000 steps, using a Langevin thermostat to regulate the temperature. In total, AMLP automatically generated 58 simulation directories, each containing the required VASP input files (INCAR, POSCAR, and KPOINTS) for 8 polymorphs evaluated at 7 distinct temperatures. These directories were fully prepared for direct submission to the computing environment, thereby eliminating the need for manual intervention during the setup stage. The only action required from the user is to provide the initial POTCAR file. From each AIMD trajectory, several configurations per polymorph were extracted, resulting in a comprehensive dataset giving both equilibrium and non-equilibrium structures as depicted in Figure 3.

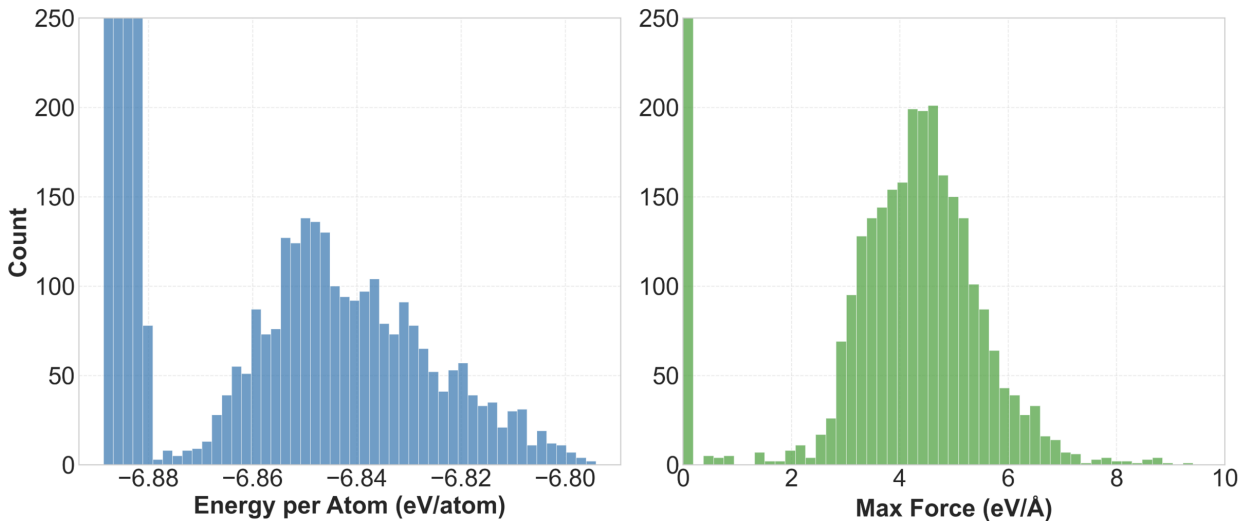


Figure 3: Distribution of the different structures coming from the DFT with (a) the energy and (b) the maximum forces.

As with the previous steps, the outputs were automatically stored by the AMLP framework, resulting in a total of 8,208 structures.

We observe a bimodal distribution, with equilibrium configurations characterized by forces in the range of 0-0.5 eV/Å, and non-equilibrium configurations spanning approximately 2-10 eV/Å. Before training, we employed the AMLP code to convert the generated `.json` files into the appropriate dataset format (HDF5). The dataset was then automatically partitioned into training and validation subsets, using an 85 % to 15 % split by default, with

a batch size of 4. Periodic boundary conditions (PBC) were identified and applied automatically during this process. To improve data quality, a force cutoff of 8 eV/Å was imposed to filter out outliers. After this preprocessing, a total of 8,108 structures remained available for model training.

3.1.2 Computational Details

Models were trained with the MACE implementation.[14] At present, users manually specify all training hyperparameters. In future releases, we will integrate LLM agents to assist with parameter selection and configuration generation. A cutoff radius of 6 Å was employed to define the local environment of each atom, ensuring the inclusion of relevant neighbors while maintaining computational efficiency.

The log loss function was chosen for its balance between sensitivity to small deviations and robustness against larger errors. The MACE fine-tuning with the foundation model mace-mpa-0-medium.model has been used. We used a foundation model, as it has been trained on the whole periodic table and on materials, making our model more flexible. Moreover, training from this checkpoint would speed up the convergence of our fitting process.[15]. We trained the models for a total of 350 epochs in two stages. During the first stage (250 epochs), equal weights were assigned to the energy and force terms. In the second stage (100 epochs), the weight on the forces was increased to be ten times larger than that on the energies, in order to prioritize force fitting. All details of the training parameters are provided in the SI.

3.1.3 Validation and tests

To assess the robustness of our results, we trained three independent committees (MACE A/B/C) using distinct random seeds. Despite their independent initialization, all three committees converged to comparable levels of accuracy, yielding mean average errors (MAEs) of approximately 7 meV/Å (equivalent to 0.67 kJ/mol) for the forces and around 2 meV/atom (0.19 kJ/mol/atom) for the energies. These values, summarized in Figure 4, highlight both the consistency across the committees and the reliability of the training procedure in reproducing reference quantum-mechanical data. These quantities are automatically computed as part of the MACE training procedure.

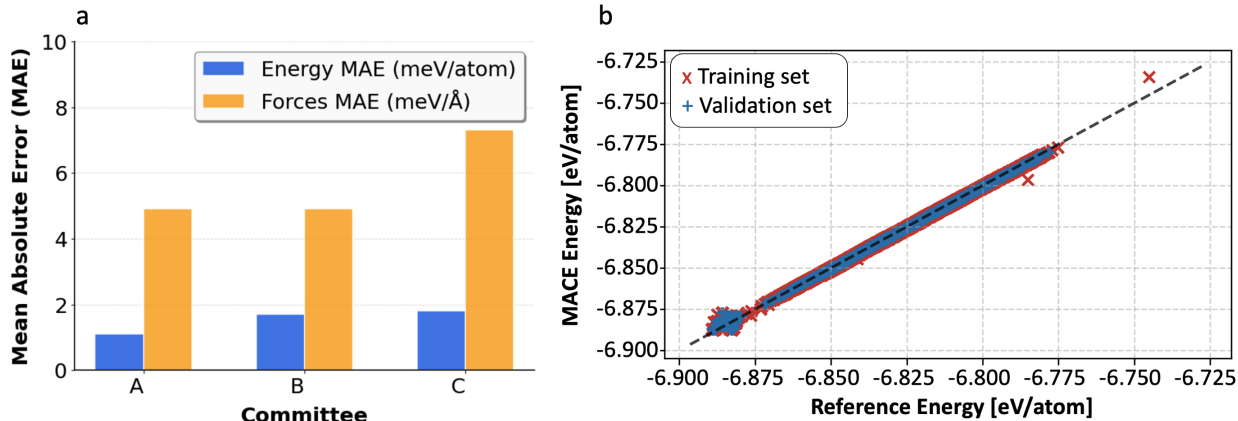


Figure 4: (a) Mean Absolute Error for the three different committees used. Comparing the MAE for energies in meV/atom (in blue) and for the forces in meV/Å (in yellow)

- (b) Correlation plots for MACE-A between the DFT reference and model energy per atom.

The errors obtained for all committees remain well below the chemical accuracy threshold of 43.36 meV (1 kcal/mol), confirming the reliability of the models. For the relative forces, the three models achieve an average error of approximately $\sim 0.97\%$ on the validation sets, further demonstrating their accuracy. The correlation between the DFT reference data and the model predictions is high for energies, as illustrated for MACE-A in Figure 4.

Further validation is conducted by performing single-point energy calculations and geometry optimizations on the relaxed structures using each committee, and comparing the results with the corresponding DFT references. Subsequently, NVE simulations are carried out to assess energy conservation for each model. Finally, NVT simulations are performed to simulate all polymorphs under different thermodynamic conditions and check their integrities. This entire procedure was carried out using the AMLP-A module, which allows users to specify the desired sequence of simulations in a simple `config.yaml` file, enabling automated execution of the selected tasks in succession.

3.1.4 Evaluation

Recovering the exact lattice-energy order of polymorphs is inherently difficult, since the uncertainties of electronic-structure methods are of comparable or even greater magnitude. Consequently, the exact order cannot be determined with confidence even at the DFT level. We therefore focus on trends, identifying which machine-learned models most consistently preserve relative stabilities and yield usable energy landscapes, rather than enforcing exact agreement with a particular DFT ranking.

To this end, we analyzed all acridine polymorphs using the AMLP framework. Two complementary protocols were employed, both starting from DFT-optimized structures: (i) single-point (SP) energy evaluations to test how closely the fitted MLIP models reproduce DFT energies on the DFT geometries, and (ii) geometry optimization (OPT) using the MLIPs (force convergence threshold 10^{-5} eV/Å. Typical OPT wall-times were 2 min per polymorph on NVIDIA A100 GPUs.

When comparing the relative lattice energies of the acridine polymorphs, we observe a comparable trend between the committees and the reference DFT calculations. In the single-point evaluations, all three committees reproduce the general energetic ordering of the polymorphs, with some quantitative deviations depending on the model. Importantly, once the polymorphs are further relaxed with geometry optimization, the agreement with DFT improves systematically. The MLIPs seem to be more successful in reproducing the relative shape of the polymorphic energy landscape than in capturing absolute lattice energies.

Across the committees, deviations from DFT increase for higher-energy polymorphs—most notably ACRDIN11 and ACRDIN04—whereas low-lying structures are reproduced with smaller errors. MACE-C is consistently the least accurate, with pronounced discrepancies on the high-energy forms; for ACRDIN04 it did not converge to a physically meaningful minimum. Geometry optimization substantially reduces single-point discrepancies and improves rank ordering, indicating that AMLP fine-tuning of MACE foundation models robustly captures the polymorphic energy landscape.

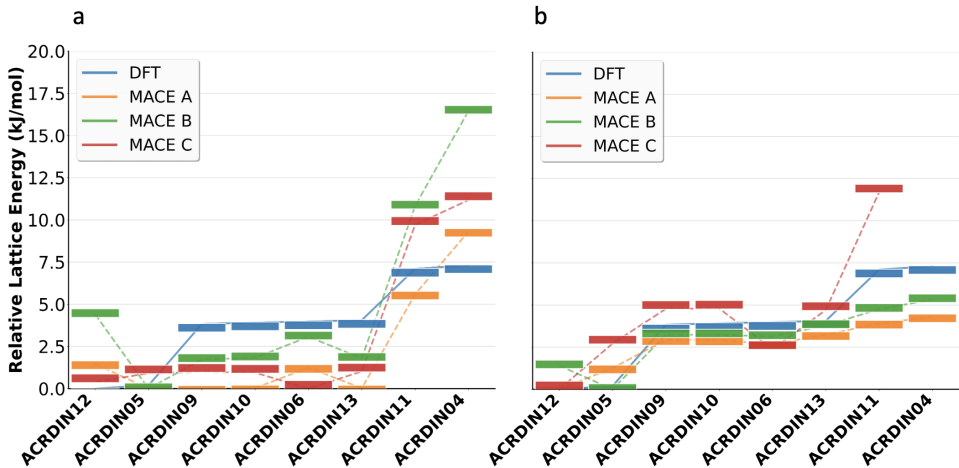


Figure 5: Comparison of relative lattice energies ($\Delta E_{\text{lattice}}$) of acridine polymorphs computed with different committees (MACE A/B/C) against DFT fully relaxed structures. (a) shows single-point evaluations, while (b) corresponds to fully relaxed geometries.

To further assess structural fidelity, we examined the RMSD of atomic positions between

DFT-relaxed structures and those obtained by geometry optimizations using the MACE models (Table 2). RMSDs were calculated after optimal structural alignment using the Kabsch algorithm, which determines the best-fit rotation and translation to superimpose the structures before computing deviations.[54, 55] All models achieve mean RMSDs of ~ 0.048 Å, indicating that the predicted and reference structures are essentially identical. MACE-C is slightly more consistent, showing lower standard deviation and maximum deviation values.

Table 2: RMSD of distances for fully DFT relaxed structures and geometry optimization for the different committees

MACE models	Mean (Å)	Std Dev (Å)	Min (Å)	Max (Å)
MACE-A	0.047	0.027	0.024	0.095
MACE-B	0.050	0.020	0.030	0.086
MACE-C	0.046	0.016	0.026	0.067

These results confirm that the three MACE committees reproduces DFT geometries with high fidelity, while capturing stability trends qualitatively even if absolute energy ranking differ.

At this stage, however, static evaluations (SP and OPT) only probe equilibrium structures and do not directly address the dynamical stability of the polymorphs under thermal conditions. A MLIP may reproduce plausible equilibrium structures while still producing unphysical trajectories when integrated over time. To establish whether the trained models generate stable and conservative dynamics consistent with their underlying potential-energy surfaces, it is therefore essential to test them under energy-conserving conditions.

Subsequently, we assessed the dynamical robustness of the trained models by performing microcanonical (NVE) simulations of 40 ps, including 1 ps equilibration, to evaluate energy conservation across the different polymorphs. The corresponding cumulative energies are summarized in Figure 6. For these simulations, all unit cells were replicated, reaching approximately 25 Å in each direction and resulting in system sizes ranging from 1,104 to 2,944 atoms, depending on the polymorph. To achieve this, a cell-replication tool was implemented within the AMLP-A module, enabling users to easily apply scaling factors along specified directions.

Across all 24 simulations (3 committees \times 8 polymorphs), the total energies are well conserved with an average energy drift consistently on the order of 10^{-4} . This performance confirms that the trained potentials are robust for energy conservation.

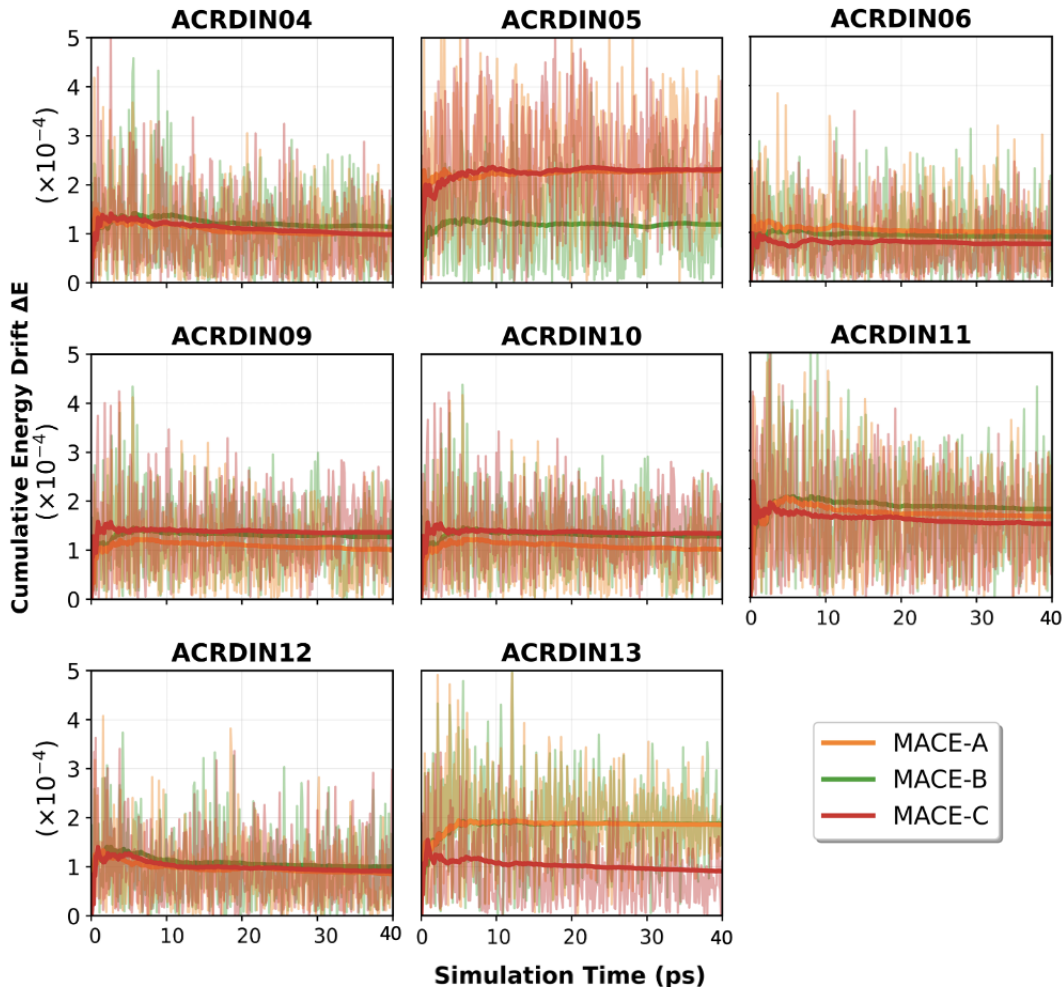


Figure 6: Cumulative energy conservation from NVE simulations of 39 ps following 1 ps of equilibration across all eight acridine polymorphs. Each panel corresponds to one polymorph, with results shown for three independently trained MLIPs: MACE-A (orange), MACE-B (green), and MACE-C (red). Solid lines represent the cumulative energy conservation, while shaded fluctuations reflect instantaneous deviations. All simulations show energy conservation on the order of 10^{-4} .

Interestingly, minor variations across polymorphs are observed. For example, ACRDIN04, ACRDIN06, ACRDIN09, ACRDIN10, ACRDIN11, and ACRDIN12 consistently exhibited very good energy conservation across all committees. By contrast, MACE-B produced the lowest variation for ACRDIN05, while MACE-C was slightly better for ACRDIN13. These subtle differences suggest that structural features of individual polymorphs may influence energy conservation.

In summary, these results confirm that the MLIPs trained within our AMLP framework provide reliable energy conservation in microcanonical simulations. With energy conservation in the 10^{-4} range, the committees establish a robust foundation for subsequent NVT

simulations and analysis of radial distribution functions (RDFs), ensuring that observed structural and thermodynamic trends are not artifacts of poor energy conservation.

To investigate the structural stability of the different polymorphs, we performed NVT simulations using the different MLIP models. Within AMLP-A, users can select among various thermostats and integrators (see Section 2.1.6). At the end of each simulation, AMLP-a automatically computes RDFs for selected atomic pairs, thereby enabling a systematic analysis of the structural evolution with temperature. In particular, C–N pairs were analyzed as a probe of intramolecular stability, while N–N pairs served to characterize intermolecular packing interactions across a temperature range of $T = 300 - 700$ K. The AMLP analysis tool was used to automatically generate the RDF plots shown in Figure 7, enabling direct comparison between different models.

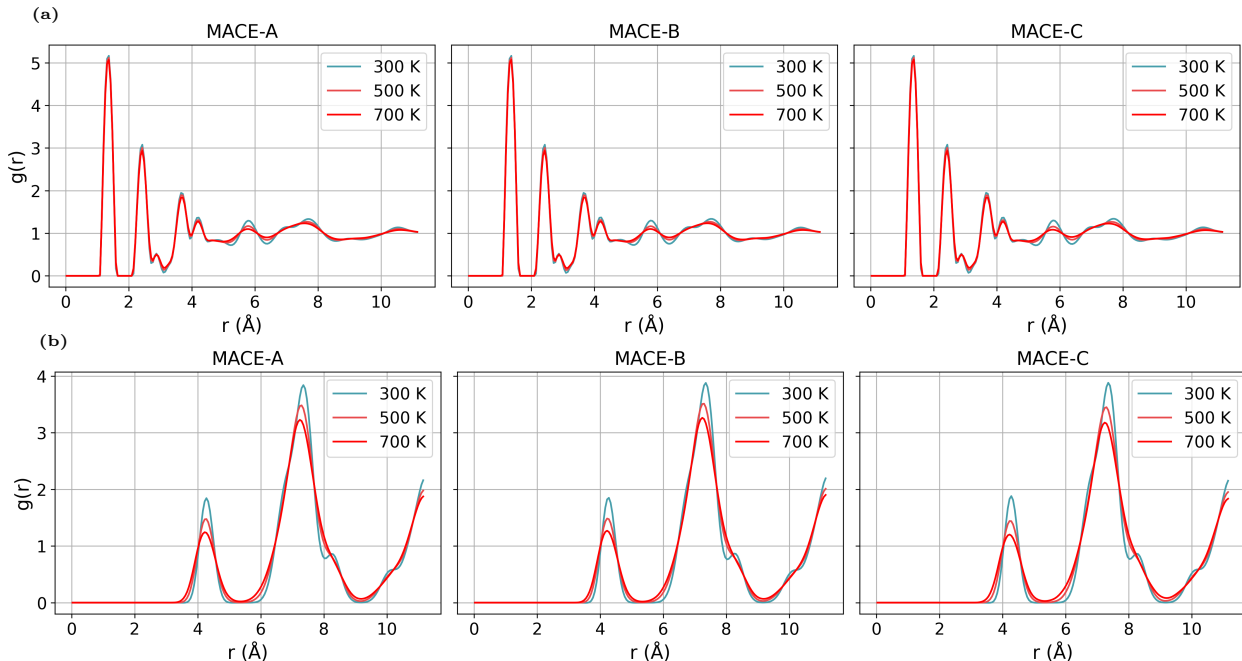


Figure 7: Radial distribution functions for ACRDIN12 at different temperatures and for different MLIP models. (a) C–N pairs. (b) N–N pairs.

The RDF for C–N pairs in Figure 7(a) has distinct peaks at approximately 1.5 Å and 2.3 Å across all three models. The peak positions remain largely unchanged with increasing temperature, but their intensities decrease and the peaks broaden with increasing temperature, reflecting the expected increase in structural disorder and reduction of long-range correlations.

For N–N pairs (Figure 7(b)), two sharp peaks at ~ 4.1 Å and ~ 7.1 Å dominate the RDFs. These features are consistently reproduced by all models and remain at fixed positions with

temperature, showing the expected thermal broadening. At higher temperatures, minor secondary peaks (e.g., around 8.5 Å and 10 Å) disappear, indicating progressive destabilization of longer-range order.

Overall, both MACE-A and MACE-B reproduce consistent thermal broadening while preserving structural integrity, as expected for stable polymorphs (see SI for additional RDF graphs). In contrast, MACE-C exhibits severe instabilities: except for ACRDIN06 and ACRDIN12, all other polymorphs become unstable above room temperature, failing to maintain stable molecular packing under thermal excitation. Such behavior is absent in MACE-A and MACE-B, which display physically reasonable RDF trends across the full temperature range.

To assess the orientational order of molecular arrangements, we employed a P_2 order parameter analysis. This functionality is not yet integrated into AMLP, but will be included in future versions. This method analyzes all molecules within our simulation cells and calculates the orientational correlation between molecular planes according to:

$$P_2 = \left\langle \frac{3 \cos^2 \theta - 1}{2} \right\rangle \quad (5)$$

where θ is the angle between molecular plane normal vectors, and the angular brackets $\langle \dots \rangle$ indicate an ensemble average over all molecular pairs. The molecular plane normal vectors are determined using principal component analysis (PCA) of atomic coordinates within each molecule, where the normal corresponds to the eigenvector with the smallest eigenvalue.

The P_2 order parameter directly reflects molecular orientations: $P_2 = 1$ indicates perfect parallel alignment, $P_2 = 0$ corresponds to random orientations, and $P_2 = -0.5$ represents perfect perpendicular alignment. Values between 0.1 – 0.2 typically indicate herringbone packing arrangements, while values above 0.5 suggest predominantly parallel packing.

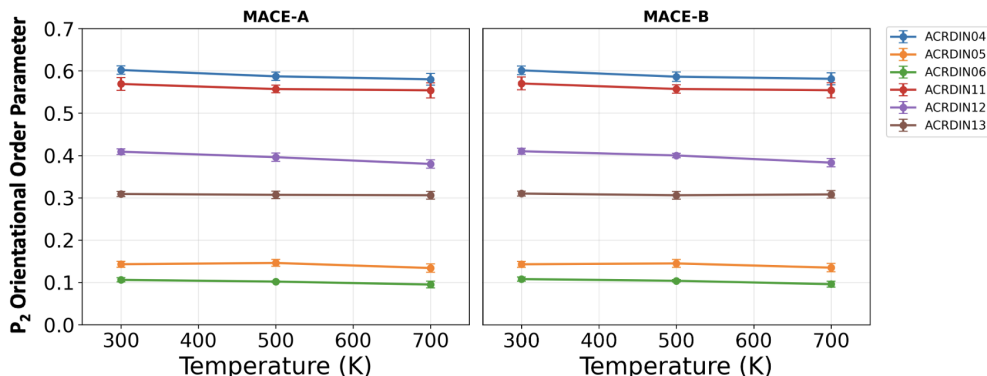


Figure 8: P_2 orientational order for acridine polymorphs at different temperatures using MACE-A and MACE-B potentials.

Figure 8 demonstrates the thermal stability and molecular packing characteristics of six acridine polymorphs across the investigated temperature range. All polymorphs exhibit modest decreases in orientational order with increasing temperature, with P_2 values typically decreasing by 0.01 – 0.02 per 200 K increase, reflecting thermal fluctuations while maintaining crystalline integrity. ACRDIN04 and ACRDIN11 show the highest P_2 values (0.58 – 0.60), indicating predominantly parallel arrangements. ACRDIN12 and ACRDIN13 exhibit intermediate values (0.38 – 0.41), suggesting mixed packing motifs with both parallel and angled molecular arrangements. ACRDIN05 and ACRDIN06 display lower P_2 values (0.14 – 0.15), characteristic of herringbone packing where molecules adopt alternating orientations. Notably, all polymorphs maintain their characteristic packing motifs across the temperature range, demonstrating preserved crystalline character and thermal stability of the molecular arrangements. The excellent agreement between MACE-A and MACE-B potentials validates the reliability of both MLIPs for predicting orientational behavior and packing motifs in molecular crystals.

4 Conclusion

In this work, we introduced AMLP, an automated machine learning pipeline designed to streamline the generation, training, and validation of MLIPs. The framework integrates LLM-driven agents for systematic dataset construction and incorporates fine-tuning procedures based on the MACE architecture.

We demonstrated the approach on acridine, a molecule with multiple known polymorphs that differ only by subtle structural variations. These simulations were computationally

intensive, requiring significant CPU and GPU resources for cell optimizations, AIMD simulations, and model training.

Our results show that the MLIPs automatically fine-tuned/trained with AMLP, achieves high accuracy, yielding close agreement with DFT references. Relative lattice energies is in agreement with DFT, rank-based stability trends are preserved. To further improve long-range accuracy, we plan to incorporate latent Ewald summation corrections into the AMLP pipeline, which explicitly address long-range electrostatics.[56]

Importantly, AMLP enables systematic validation of trained MLIPs against DFT geometries, which are reproduced with sub-Å accuracy, confirming structural fidelity. The framework further automates dynamical assessments: under NVE conditions, trajectories remain stable and conservative with energy conservation better than 0.01%. Subsequent NVT simulations and analyses demonstrate that AMLP provides a consistent framework for evaluating structural correlations across a wide range of temperatures. This enables a direct assessment of model quality, particularly in terms of their robustness in molecular dynamics simulations, and reveals distinct differences in performance between the MLIPs.

These findings emphasize the importance of dynamical validation, as equilibrium accuracy alone may be insufficient to guarantee model robustness at finite temperature. The AMLP pipeline simplifies this entire process, lowering the barrier of entry for researchers who are new to machine-learned interatomic potentials.

The current AMLP framework represents a first complete version including the most important functionalities for an automated fine-tuning and fitting of MLIPs. Future developments will focus on expanding usability, for instance, by enabling LLM agents to directly generate plots or analyze `.json` datasets on demand, as recently demonstrated for agentized scientific workflows.[57] We also plan to extend support beyond MACE to other state-of-the-art models such as NequIP[58], TorchMD[59], and FeNNol[60], thereby broadening AMLP’s applicability and robustness in computational materials science and theoretical chemistry.

Acknowledgments

Author Contributions

Adam Lahouari (ORCID: 0000-0001-5857-1066), Jutta Rogal (ORCID:0000-0002-6268-380X) and Mark E. Tuckerman (ORCID: 0000-0003-2194-9955) conceived and designed the study. Adam Lahouari developed the code, performed the computational experiments, analyzed the data, and drafted the manuscript. Jutta Rogal and Mark E. Tuckerman contributed to the writing and revision of the manuscript. All authors gave final approval for the version to be

published.

Funding

This work was supported by the National Science Foundation grant DMR-2118890. JR acknowledges financial support from the Deutsche Forschungsgemeinschaft (DFG) through the Heisenberg Programme project 428315600. The Flatiron Institute is a division of the Simons Foundation. This work was supported in part through the NYU IT High Performance Computing resources, services, and staff expertise.

Conflicts of Interest

The authors declare no competing interests.

Data Availability

All data are available on the github of Adam Lahouari at <https://github.com/adamlaho/AMLP>

Supplementary Materials

The supplementary material is included below.

References

- [1] Kim, J.; Liu, Y.; Luo, T.; Tian, Z. Molecular dynamics simulations in nanoscale heat transfer: a mini review. *ASME J. Heat Mass Transfer* **2025**, *147*, 030801.
- [2] Zhou, X. W.; Heo, T. W.; Wood, B. C.; Stavila, V.; Kang, S.; Allendorf, M. D. Finite-temperature behavior of PdH_x elastic constants computed by direct molecular dynamics. *MRS Adv.* **2017**, *2*, 3341–3346.
- [3] Greener, J. G. Differentiable simulation to develop molecular dynamics force fields for disordered proteins. *Chem. Sci.* **2024**, *15*, 4897–4909.
- [4] Parks, C.; Koswara, A.; DeVilbiss, F.; Tung, H.-H.; Nere, N. K.; Bordawekar, S.; Nagy, Z. K.; Ramkrishna, D. Solubility curves and nucleation rates from molecular dynamics for polymorph prediction – moving beyond lattice energy minimization. *Phys. Chem. Chem. Phys.* **2017**, *19*, 5285–5295.

- [5] Francia, N. F.; Price, L. S.; Salvalaglio, M. Reducing crystal structure overprediction of ibuprofen with large scale molecular dynamics simulations. *CrystEngComm* **2021**, *23*, 5575–5584.
- [6] Chmiela, S.; Sauceda, H. E.; Müller, K.-R.; Tkatchenko, A. Towards exact molecular dynamics simulations with machine-learned force fields. *Nat. Commun.* **2018**, *9*, 3887.
- [7] Bogojeski, M.; Vogt-Maranto, L.; Tuckerman, M. E.; Müller, K.-R.; Burke, K. Quantum chemical accuracy from density functional approximations via machine learning. *Nat. Commun.* **2020**, *11*, 5223.
- [8] Peterson, G. G. C.; Brgoch, J. Materials discovery through machine learning formation energy. *J. Phys. Energy* **2021**, *3*, 022002.
- [9] Park, Y.; Kim, J.; Hwang, S.; Han, S. Scalable parallel algorithm for graph neural network interatomic potentials in molecular dynamics simulations. *J. Chem. Theory Comput.* **2024**, *20*, 4857–4868.
- [10] Batzner, S.; Musaelian, A.; Sun, L.; Geiger, M.; Mailoa, J. P.; Kornbluth, M.; Molinari, N.; Smidt, T. E.; Kozinsky, B. E(3)-equivariant graph neural networks for data-efficient and accurate interatomic potentials. *Nat. Commun.* **2022**, *13*, 2453.
- [11] Dunn, A.; Wang, Q.; Ganose, A.; Dopp, D.; Jain, A. Benchmarking materials property prediction methods: the Matbench test set and Automatminer reference algorithm. *npj Comput. Mater.* **2020**, *6*, 138.
- [12] Riebesell, J.; Goodall, R. E. A.; Benner, P.; Chiang, Y.; Deng, B.; Ceder, G.; Asta, M.; Lee, A. A.; Jain, A.; Persson, K. A. Matbench discovery: a framework to evaluate machine learning crystal stability predictions. *Nat. Mach. Intell.* **2025**, *7*, 192–204.
- [13] Gharakhanyan, V. et al. Open molecular crystals 2025 (OMC25) dataset and models. *arXiv preprint* **2025**, arXiv:2508.02651.
- [14] Batatia, I.; Kovács, D. P.; Simm, G. N. C.; Ortner, C.; Csányi, G. MACE: higher order equivariant message passing neural networks for fast and accurate force fields. *arXiv preprint* **2023**, arXiv:2206.07697.
- [15] Della Pia, F.; Shi, B. X.; Kapil, V.; Zen, A.; Alfè, D.; Michaelides, A. Accurate and efficient machine learning interatomic potentials for finite temperature modeling of molecular crystals. *arXiv preprint* **2025**, arXiv:2502.15530.

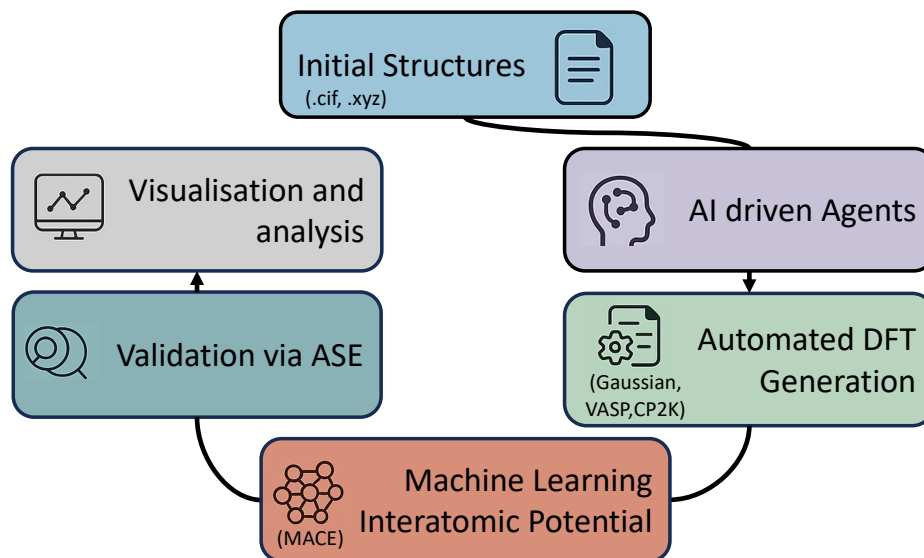
- [16] Frisch, M. J. et al. Gaussian 16 Revision C.01. 2016; Gaussian Inc., Wallingford, CT.
- [17] Kresse, G.; Hafner, J. Ab initio molecular dynamics for liquid metals. *Phys. Rev. B* **1993**, *47*, 558–561.
- [18] Kresse, G.; Hafner, J. Norm-conserving and ultrasoft pseudopotentials for first-row and transition elements. *J. Phys. Condens. Matter* **1994**, *6*, 8245.
- [19] Kresse, G.; Furthmüller, J. Efficiency of ab-initio total energy calculations for metals and semiconductors using a plane-wave basis set. *Comput. Mater. Sci.* **1996**, *6*, 15–50.
- [20] Kresse, G.; Furthmüller, J. Efficient iterative schemes for ab initio total-energy calculations using a plane-wave basis set. *Phys. Rev. B* **1996**, *54*, 11169–11186.
- [21] Kühne, T. D. et al. CP2K: an electronic structure and molecular dynamics software package—Quickstep: efficient and accurate electronic structure calculations. *J. Chem. Phys.* **2020**, *152*, 194103.
- [22] Larsen, A. H. et al. The atomic simulation environment—a Python library for working with atoms. *J. Phys. Condens. Matter* **2017**, *29*, 273002.
- [23] Lahouari, A. Introduction to Automated Machine Learning Pipeline - Google Colab Tutorial. 2025; <https://drive.google.com/file/d/11P108iQei8LeZ-H-4Vvvit0qrBGUqNFb/view?usp=sharing>, Accessed: September 29, 2025.
- [24] Mirza, A. et al. A framework for evaluating the chemical knowledge and reasoning abilities of large language models against the expertise of chemists. *Nat. Chem.* **2025**, *17*, 1–8.
- [25] Schmidgall, S.; Su, Y.; Wang, Z.; Sun, X.; Wu, J.; Yu, X.; Liu, J.; Moor, M.; Liu, Z.; Barsoum, E. Agent laboratory: using LLM agents as research assistants. *arXiv preprint* **2025**, arXiv:2501.04227.
- [26] Pham, T. D.; Tanikanti, A.; Keçeli, M. ChemGraph: an agentic framework for computational chemistry workflows. *arXiv preprint* **2025**, arXiv:2506.06363.
- [27] Cornell University arXiv preprint server. 1991; <https://arxiv.org>, Open access e-print archive.
- [28] Crossref Crossref DOI registration agency. 2000; <https://www.crossref.org>, Digital object identifier registration and metadata services.

- [29] National Center for Biotechnology Information PubMed. 1996; <https://pubmed.ncbi.nlm.nih.gov>, Biomedical literature database, U.S. National Library of Medicine.
- [30] Allen Institute for AI Semantic Scholar. 2015; <https://www.semanticscholar.org>, AI-powered academic search engine.
- [31] Lahouari, A. AMLP: Automated Machine Learning Pipeline. 2025; <https://github.com/adamlaho/AMLP>, GitHub repository.
- [32] Broyden, C. G. The convergence of a class of double-rank minimization algorithms. *J. Inst. Math. Appl.* **1970**, *6*, 76–90.
- [33] Fletcher, R. A new approach to variable metric algorithms. *Comput. J.* **1970**, *13*, 317–322.
- [34] Goldfarb, D. A family of variable-metric methods derived by variational means. *Math. Comput.* **1970**, *24*, 23–26.
- [35] Shanno, D. F. Conditioning of quasi-Newton methods for function minimization. *Math. Comput.* **1970**, *24*, 647–656.
- [36] Liu, D. C.; Nocedal, J. On the limited memory BFGS method for large scale optimization. *Math. Program.* **1989**, *45*, 503–528.
- [37] Bitzek, E.; Koskinen, P.; Gähler, F.; Moseler, M.; Gumbusch, P. Structural relaxation made simple. *Phys. Rev. Lett.* **2006**, *97*, 170201.
- [38] ASE Developers ASE: Atomic Simulation Environment documentation. 2024; <https://wiki.fysik.dtu.dk/ase/>, Online documentation, accessed [Date].
- [39] Schneider, T.; Stoll, E. Molecular-dynamics study of a three-dimensional one-component model for distortive phase transitions. *Phys. Rev. B* **1978**, *17*, 1302–1322.
- [40] Nosé, S. A unified formulation of the constant temperature molecular dynamics methods. *J. Chem. Phys.* **1984**, *81*, 511–519.
- [41] Hoover, W. G. Canonical dynamics: equilibrium phase-space distributions. *Phys. Rev. A* **1985**, *31*, 1695–1697.
- [42] Tuckerman, M. E. *Statistical mechanics: theory and molecular simulation*, 2nd ed.; Oxford University Press: Oxford, 2023.

- [43] McGibbon, R. T.; Beauchamp, K. A.; Harrigan, M. P.; Klein, C.; Swails, J. M.; Hernández, C. X.; Schwantes, C. R.; Wang, L.-P.; Lane, T. J.; Pande, V. S. MDTraj: A modern open library for the analysis of molecular dynamics trajectories. *Biophys. J.* **2015**, *109*, 1528–1532.
- [44] Schur, E.; Bernstein, J.; Price, L. S.; Guo, R.; Price, S. L.; Lapidus, S. H.; Stephens, P. W. The (current) acridine solid form landscape: eight polymorphs and a hydrate. *Cryst. Growth Des.* **2019**, *19*, 4884–4893.
- [45] Nyman, J.; Day, G. M. Static and lattice vibrational energy differences between polymorphs. *CrystEngComm* **2015**, *17*, 5154–5165.
- [46] Price, S. L. Computational prediction of organic crystal structures and polymorphism. *Int. Rev. Phys. Chem.* **2008**, *27*, 541–568.
- [47] Perdew, J. P.; Burke, K.; Ernzerhof, M. Generalized gradient approximation made simple. *Phys. Rev. Lett.* **1996**, *77*, 3865–3868.
- [48] Monkhorst, H. J.; Pack, J. D. Special points for Brillouin-zone integrations. *Phys. Rev. B* **1976**, *13*, 5188–5192.
- [49] Grimme, S.; Ehrlich, S.; Goerigk, L. Effect of the damping function in dispersion corrected density functional theory. *J. Comput. Chem.* **2011**, *32*, 1456–1465.
- [50] Caldeweyher, E.; Mewes, J.-M.; Ehlert, S.; Grimme, S. Extension and evaluation of the D4 London-dispersion model for periodic systems. *Phys. Chem. Chem. Phys.* **2020**, *22*, 8499–8512.
- [51] Firaha, D. et al. Predicting crystal form stability under real-world conditions. *Nature* **2023**, *623*, 324–328.
- [52] Hoja, J.; Tkatchenko, A. First-principles stability ranking of molecular crystal polymorphs with the DFT+MBD approach. *Faraday Discuss.* **2018**, *211*, 253–274.
- [53] Hoja, J.; Ko, H.-Y.; Neumann, M. A.; Car, R.; DiStasio, R. A.; Tkatchenko, A. Reliable and practical computational description of molecular crystal polymorphs. *Sci. Adv.* **2019**, *5*, eaau3338.
- [54] Kabsch, W. A discussion of the solution for the best rotation to relate two sets of vectors. *Acta Crystallographica Section A* **1978**, *34*, 827–828.

- [55] Kabsch, W. Protein structure similarities. *Acta Crystallographica Section A* **2001**, *11*, 348–353.
- [56] Kim, D.; Wang, X.; Zhong, P.; King, D. S.; Inizan, T. J.; Cheng, B. A universal augmentation framework for long-range electrostatics in machine learning interatomic potentials. *arXiv preprint* **2025**, arXiv:2507.14302.
- [57] Wang, Z.; Huang, H.; Zhao, H.; Xu, C.; Zhu, S.; Janssen, J.; Viswanathan, V. DREAMS: density functional theory based research engine for agentic materials simulation. *arXiv preprint* **2025**, arXiv:2507.14267.
- [58] Batzner, S.; Musaelian, A.; Sun, L.; Geiger, M.; Mailoa, J. P.; Kornbluth, M.; Molinari, N.; Smidt, T. E.; Kozinsky, B. E(3)-equivariant graph neural networks for data-efficient and accurate interatomic potentials. *Nat. Commun.* **2022**, *13*, 2453.
- [59] Doerr, S.; Majewski, M.; Pérez, A.; Krämer, A.; Clementi, C.; Noe, F.; Giorgino, T.; De Fabritiis, G. TorchMD: a deep learning framework for molecular simulations. *J. Chem. Theory Comput.* **2021**, *17*, 2355–2363.
- [60] Plé, T.; Adjoua, O.; Lagardère, L.; Piquemal, J.-P. FeNNol: an efficient and flexible library for building force-field-enhanced neural network potentials. *J. Chem. Phys.* **2024**, *161*, 042502.

TOC Graphic



Supporting Information:

Automated Machine Learning Pipeline for training and analysis using Large language models

Adam Lahouari,¹ Jutta Rogal,^{1,2} and Mark E. Tuckerman^{1,3,4,5,6}

¹New York University, Department of Chemistry, New York, New York 10003, USA

²Initiative for Computational Catalysis, Flatiron Institute, New York, New York 10010, USA

³New York University, Department of Physics, New York, New York 10003, USA

⁴Courant Institute of Mathematical Sciences, New York University, New York, New York 10012, USA

⁵NYU-ECNU Center for Computational Chemistry at NYU Shanghai, Shanghai 200062, China

⁶Simons Center for Computational Physical Chemistry, Department of Chemistry, New York 10003, USA

E-mail: al9500@nyu.edu

Key Findings from AMLP Literature Analysis

Table S1 summarizes the major insights identified by the multi-agent literature analysis, with direct links to the retrieved publications and expert assessments.

Table S1: Key findings from AMLP multi-agent literature analysis for acridine polymorph research.

Finding Category	Key Insight	Source & Evidence
Acridine Literature	Limited direct studies on acridine polymorphs	Experimental & theoretical reports: no specific acridine polymorph literature found
Crystal Structure Prediction	AlphaCrystal-II deep learning approach	arXiv:2404.04810v1 – distance matrix-based crystal prediction
Experimental Techniques	PXRD for crystal characterization	arXiv:2401.03862v3 – end-to-end crystal structure prediction from PXRD
Novel Analysis Methods	Inverse EXAFS Analysis (IEA)	arXiv:2409.09693v1 – comparative study with Demeter software
Materials Discovery	Autonomous ML-driven discovery	arXiv:2508.02956v1 – multi-agent physics-aware reasoning
Similar Systems	Aromatic heterocycle precedents	Theoretical report: anthracene, phenanthrene, quinoline as model systems
Computational Gaps	DFT + ML integration needed	All expert reports: lack of systematic acridine polymorph studies
Methodology Limitations	Self-interaction error in DFT	Gaussian expert: arXiv:2412.18350v1 – exchange-correlation functionals
Software Capabilities	VASP for solid-state calculations	VASP expert: arXiv:2508.07035v1 – VASPIlot automation platform
Force Field Development	Neural network potential comparison	VASP expert: arXiv:2304.10820v1 – Matlantis vs VASP comparison

Research Opportunity Assessment

Based on the literature analysis, AMLP identified several research opportunities:

Table S2: Research gaps and opportunities identified by AMLP for acridine ML potential development.

Gap Type	Specific Opportunity	Recommended Approach
Experimental Data	Acridine polymorph characterization	Systematic PXRD and thermal analysis studies
Computational Benchmark	DFT method validation for acridine	Compare PBE, PBE-D3(BJ), hybrid functionals
ML Architecture	Neural network potential training	Combine VASP DFT data with modern ML frameworks
Phase Transition	Thermodynamic modeling	Free energy calculations using enhanced sampling
Software Integration	Automated workflow development	Extend VASPilot-type approaches to polymorph screening
Validation Framework	Experimental-computational synergy	Cross-validate ML predictions with crystal growth experiments

Table S3: Actual AMLP DFT-parameter recommendations for acridine crystalline systems.

Software	Parameter	Recommended Value & Provenance
VASP	ENCUT	500 eV (molecular systems literature)
	XC functional	PBE (standard for organic crystals)
	Method focus	Periodic DFT with dispersion corrections
Gaussian	Method	B3LYP (organic chemistry standard)
	Basis set	6-31G(d,p) (balanced accuracy/cost)
	Application	Molecular property benchmarking
CP2K	XC functional	PBE (consistent with VASP)
	Basis set	DZVP-MOLOPT-SR-GTH
	Method	Mixed Gaussian/plane-wave (GPW)
General	Dispersion	D3(BJ) corrections recommended
	Convergence	10^{-6} eV electronic, 10^{-3} eV \AA^{-1} forces

Computational Methods

Density Functional Theory (DFT) Calculations

All DFT calculations were performed using the Vienna Ab initio Simulation Package (VASP) with the Projector Augmented Wave (PAW) method.[17–20] In this study on acridine, we decided to use VASP with the following parameters:

Cell Optimization Parameters

Table S4: VASP parameters for cell optimization

Parameter	Value	Description
SYSTEM	acridine_cell	System identifier
ALGO	Normal	Electronic minimization algorithm
EDIFF	1×10^{-6} eV	Electronic convergence criterion
ENCUT	850.0 eV	Plane-wave cutoff energy
GGA	PE	Exchange-correlation functional (PBE)
IBRION	2	Ionic relaxation algorithm (conjugate gradient)
ISIF	3	Stress tensor calculation (cell shape and volume optimization)
ISMEAR	-1	Smearing method (Fermi smearing)
IVDW	13	van der Waals correction method
KPOINTS	$7 \times 7 \times 7$	K-point mesh (Gamma-centered, automatic)
LCHARG	.TRUE.	Write charge density
LREAL	Auto	Real-space projection
LVDW	.TRUE.	Enable van der Waals corrections
LWAVE	.TRUE.	Write wavefunctions
NELM	100	Maximum electronic self-consistency steps
NSW	150	Maximum ionic relaxation steps
PREC	High	Precision level
SIGMA	0.05 eV	Smearing parameter
VDW_R0	12.0 Å	van der Waals cutoff radius

Ab Initio Molecular Dynamics (AIMD) Parameters

For the AIMD, the following parameters were used for different temperature:

Table S5: Molecular dynamics control parameters for AIMD simulation at 300 K

Parameter	Value	Description
IBRION	0	Molecular dynamics mode
NSW	10,000	Number of MD steps
POTIM	1.0 fs	Time step
TEBEG	300.0 K	Initial temperature
TEEND	300.0 K	Final temperature
ISYM	0	Symmetry disabled for MD
MDALGO	3	Langevin thermostat
ISIF	2	Stress tensor calculation (ionic positions only)

Langevin Thermostat Parameters:

- **LANGEVIN_GAMMA:** 10.0 10.0 10.0 (friction coefficients for N, C, H atoms)
- **LANGEVIN_GAMMA_L:** 1.0 (lattice friction coefficient)
- Species-specific friction coefficients: N: $\gamma = 10.0$ THz, C: $\gamma = 10.0$ THz, H: $\gamma = 10.0$ THz

Table S6: Electronic structure and algorithm parameters for AIMD

Parameter	Value	Description
ENCUT	850.0 eV	Plane-wave cutoff energy
EDIFF	1×10^{-6} eV	Electronic convergence criterion
NELM	100	Maximum electronic steps
ISMEAR	-1	Fermi smearing
SIGMA	0.05 eV	Smearing parameter
GGA	PE	PBE exchange-correlation functional
LVDW	.TRUE.	Enable van der Waals corrections
IVDW	13	van der Waals method
VDW_R0	8.0 Å	van der Waals cutoff radius
PREC	High	Precision level
ALGO	Fast	Electronic minimization algorithm
LREAL	Auto	Real-space projection
LWAVE	.FALSE.	Do not write wavefunctions
LCHARG	.FALSE.	Do not write charge density
NBLOCK	1	Output frequency
KBLOCK	10	k-point output frequency
LCHIMAG	.FALSE.	Magnetic moments output

Machine Learning Model Training

Data Preparation

For the training dataset preparation:

- **Force cutoff:** 10.0 eV Å⁻¹ (configurations with forces exceeding this threshold were excluded from training)
- **Atomic species:** H ($Z = 1$), C ($Z = 6$), N ($Z = 7$)
- **Data split:** 85% training, 15% validation

MACE Model Configuration

The Machine learning Atomic Cluster Expansion (MACE) model was trained using a foundation model approach with the following configuration:

Table S7: MACE model architecture and training parameters

Parameter	Value	Description
Foundation Model Settings		
foundation_model	mace-mpa-0-medium.model	Base pre-trained model
multiheads_finetuning	False	Transfer learning approach
Model Architecture		
num_channels	128	Number of hidden channels
max_L	2	Maximum angular momentum
num_interactions	2	Number of interaction layers
correlation	3	Correlation order
max_ell	3	Maximum spherical harmonic degree
r_max	6.0 Å	Cutoff radius
Training Parameters		
device	cuda	Training device
batch_size	12	Training batch size
max_num_epochs	350	Maximum training epochs
default_dtype	float64	Numerical precision
Optimization Settings		
swa	True	Stochastic Weight Averaging
start_swa	250	SWA start epoch
swa_lr	0.0001	SWA learning rate
swa_forces_weight	10	SWA forces weight
swa_energy_weight	1	SWA energy weight
ema	True	Exponential Moving Average
ema_decay	0.99	EMA decay rate
amsgrad	True	AMSGrad optimizer variant
Loss Function and Scaling		
loss	ef	Energy and forces loss
scaling	rms_forces_scaling	Force scaling method
error_table	PerAtomMAE	Error metric

Atomic Reference Energies

Table S8: Atomic reference energies (E0s) used in MACE training

Element	Energy (eV)
H	-0.27737421
C	-0.77091629
N	-0.83778712

Ensemble Training

To ensure robustness and estimate model uncertainty, three independent models were trained using different random seeds with identical hyperparameters:

- **Seeds:** 49, 67, 127
- **Training epochs:** 300 epochs each
- **Committee approach:** All models trained with identical hyperparameters to form an ensemble for improved prediction accuracy and uncertainty quantification
- **Total number of parameters:** 752,174

Supplementary Figures

Radial Distribution Functions: C–N pairs

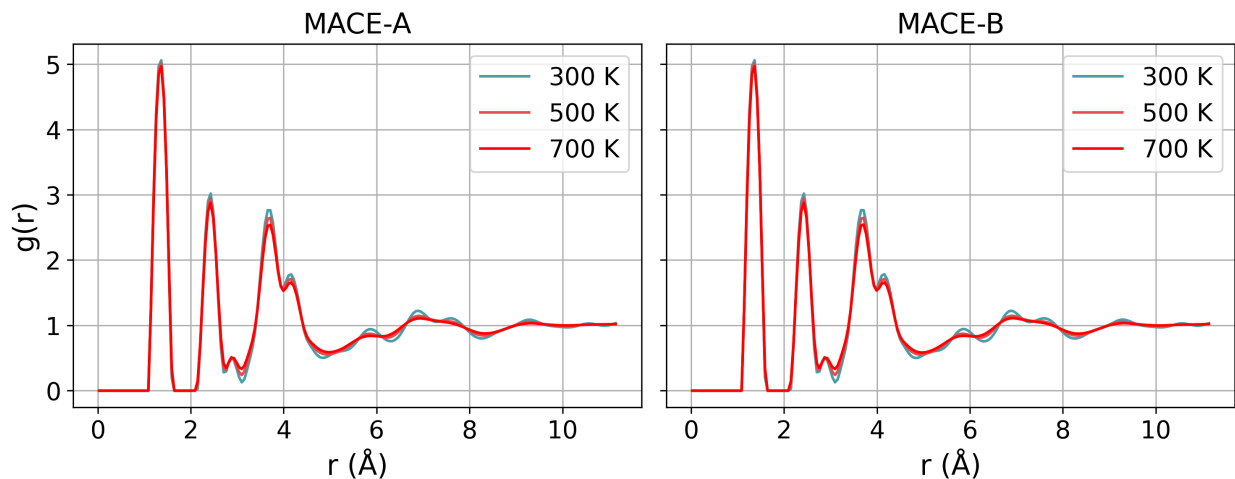


Figure S1: C–N pair radial distribution function $g_{\text{C-N}}(r)$ for ACRDIN04 acridine polymorph.

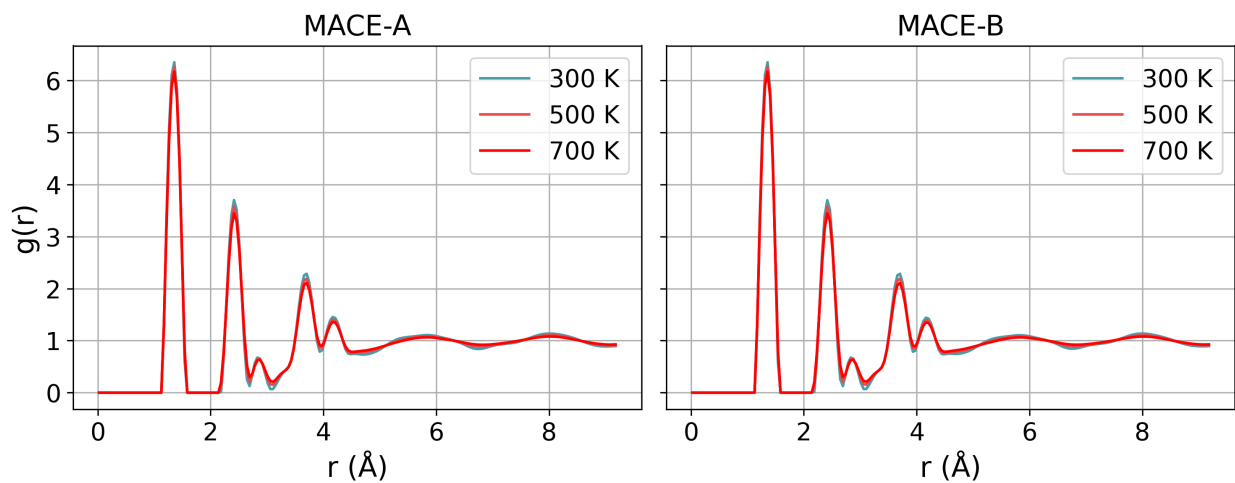


Figure S2: C–N pair radial distribution function $g_{\text{C-N}}(r)$ for ACRDIN05 acridine polymorph.

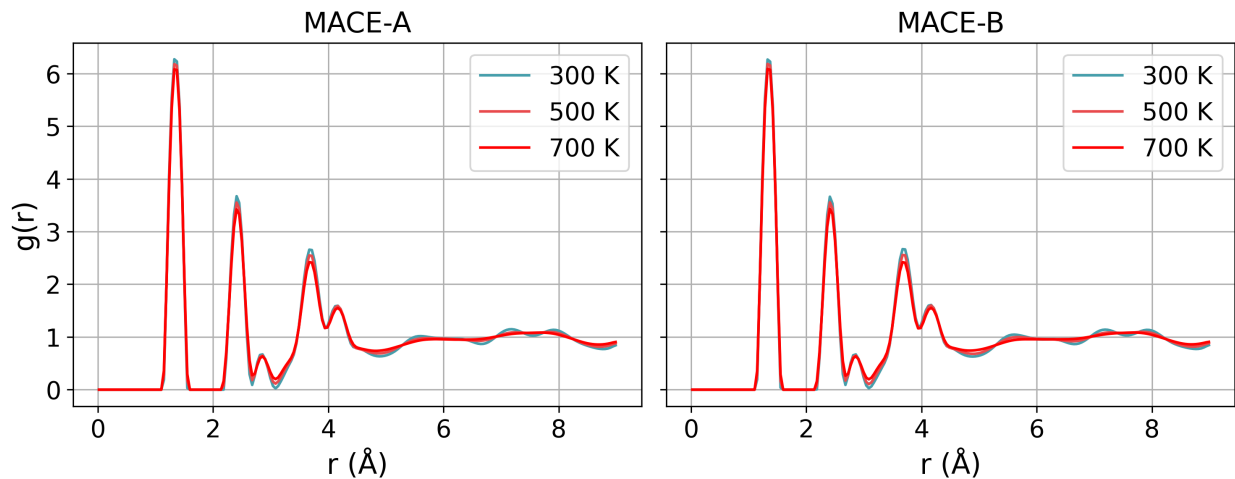


Figure S3: C-N pair radial distribution function $g_{C-N}(r)$ for ACRDIN06 acridine polymorph.

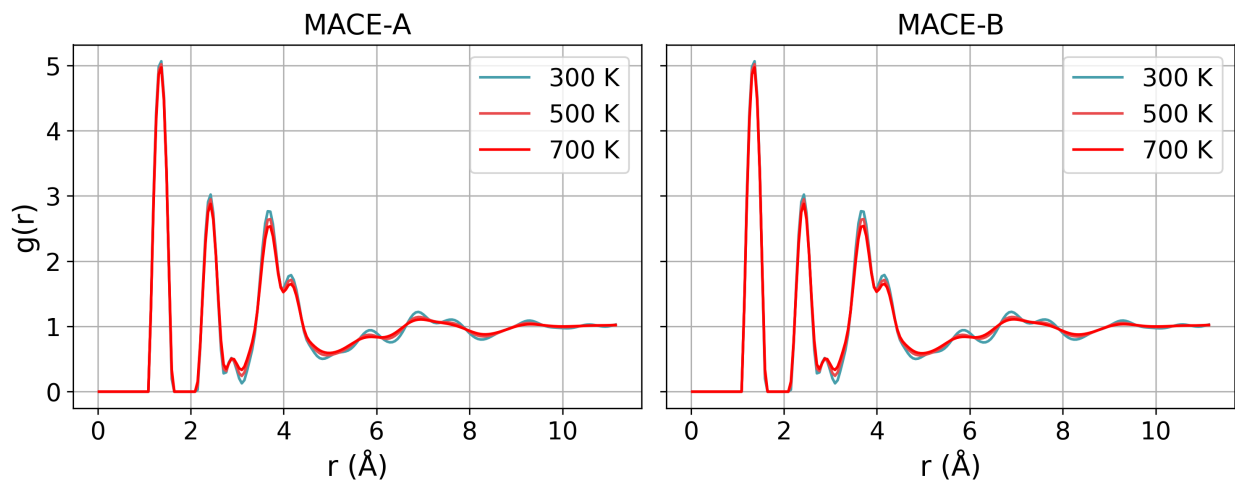


Figure S4: C-N pair radial distribution function $g_{C-N}(r)$ for ACRDIN11 acridine polymorph.

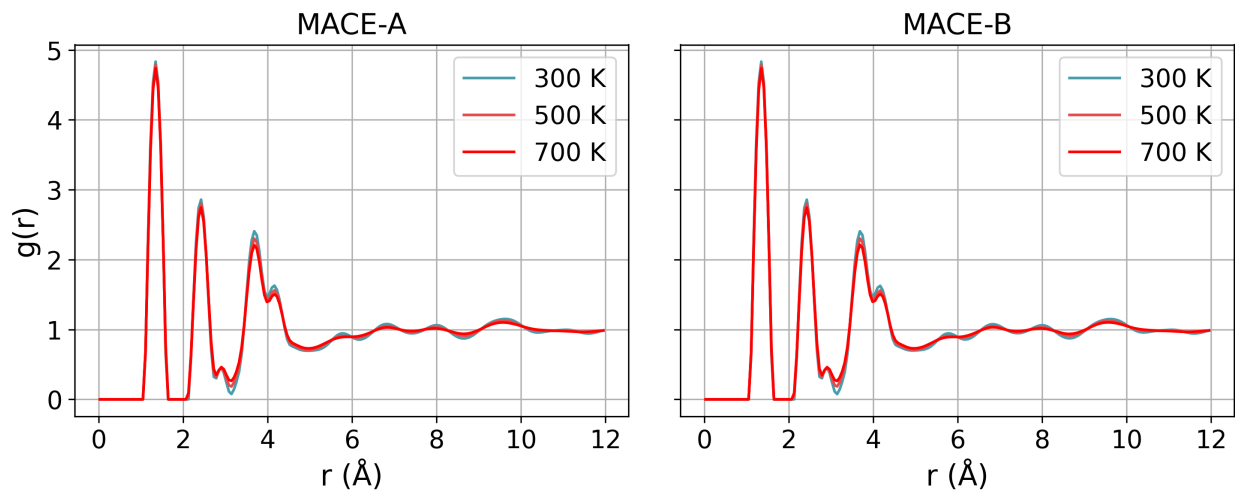


Figure S5: C–N pair radial distribution function $g_{\text{C-N}}(r)$ for ACRDIN13 acridine polymorph.

Radial Distribution Functions: N–N pairs

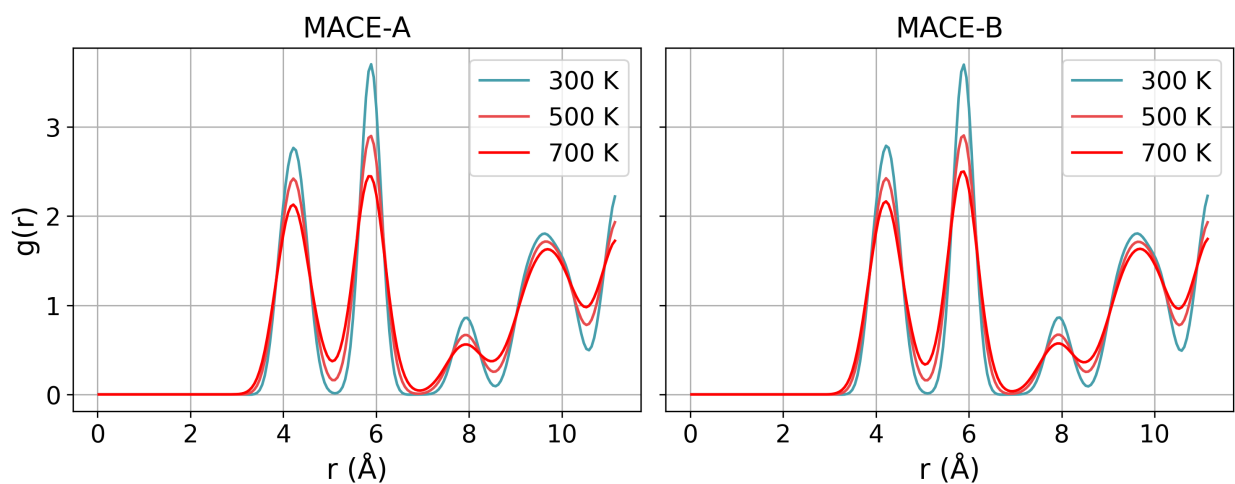


Figure S6: N–N pair radial distribution function $g_{\text{N-N}}(r)$ for ACRDIN04 acridine polymorph.

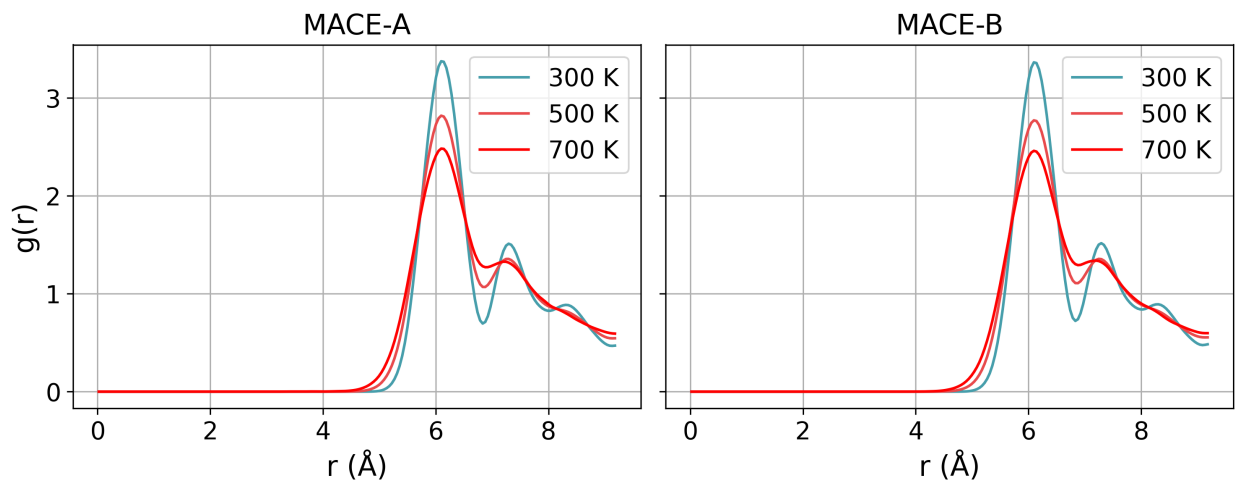


Figure S7: N–N pair radial distribution function $g_{N-N}(r)$ for ACRDIN05 acridine polymorph.

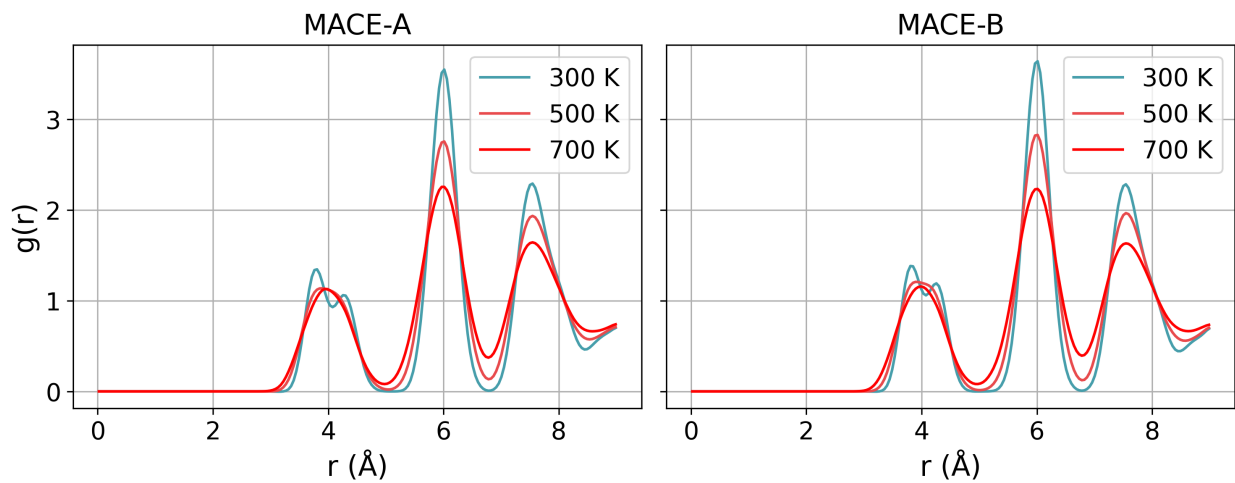


Figure S8: N–N pair radial distribution function $g_{N-N}(r)$ for ACRDIN06 acridine polymorph.

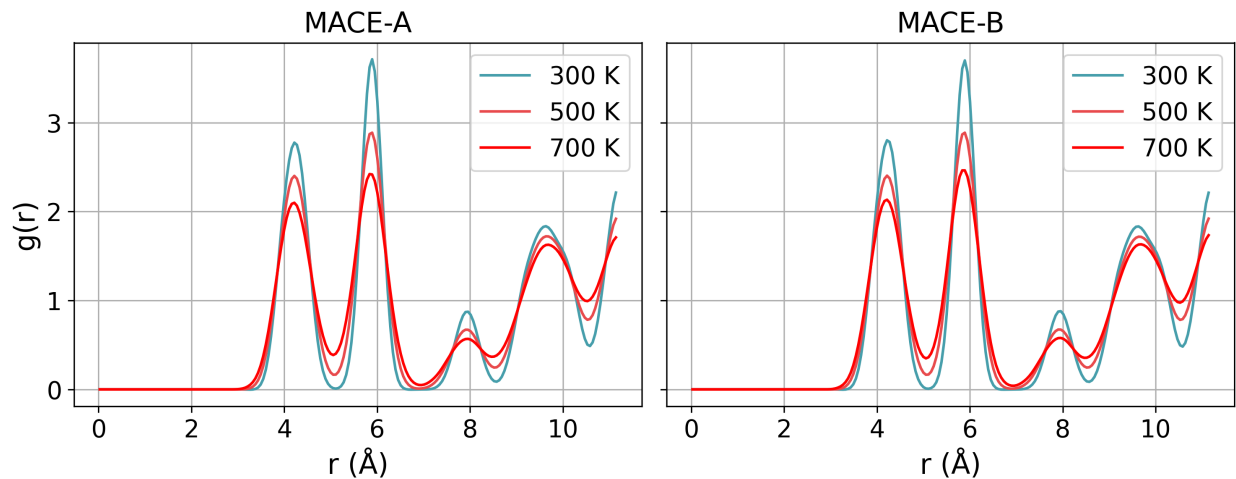


Figure S9: N–N pair radial distribution function $g_{N-N}(r)$ for ACRDIN11 acridine polymorph.

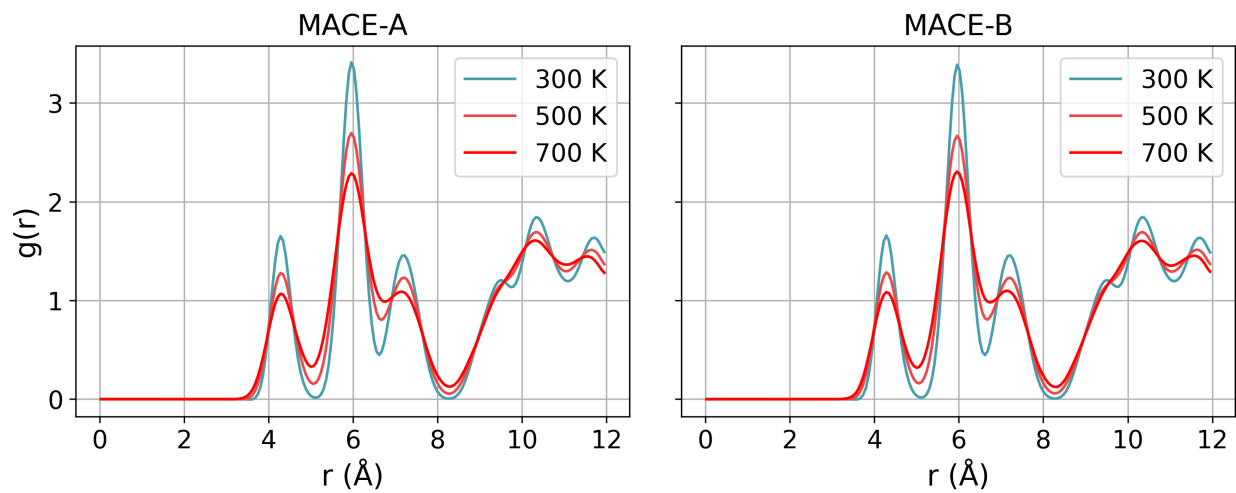


Figure S10: N–N pair radial distribution function $g_{N-N}(r)$ for ACRDIN13 acridine polymorph.